



TECHNISCHE  
UNIVERSITÄT  
WIEN

MASTER THESIS

# Energy approach to analysis of natural oscillations of plates with cracks or added masses

carried out for the purpose of obtaining the degree of Diplom-Ingenieur  
submitted at TU Wien, Faculty of Mechanical and Industrial Engineering by

**Roman BUCHTA, BSc**

Mat. Nr. 11734313

under the supervision of

Univ.Prof. Mag. Dr. Yury Vetyukov

Institute of Mechanics and Mechatronics

E325-02 - Research Unit of Mechanics of Solids

Leobersdorf, in October 2024

I confirm that the printing of this thesis under the title  
**master thesis**  
requires the approval of the examination board.

### **Affidavit**

I declare in lieu of oath, that I wrote this thesis and carried out the associated research myself, using only the literature cited in this volume. If text passages from sources are used literally, they are marked as such.

I confirm that this work is original and has not been submitted for examination elsewhere, nor is it currently under consideration for a thesis elsewhere.

I acknowledge that the submitted work will be checked electronically-technically using suitable and state-of-the-art means (plagiarism detection software). On the one hand, this ensures that the submitted work was prepared according to the high-quality standards within the applicable rules to ensure good scientific practice "Code of Conduct" at the TU Wien. On the other hand, a comparison with other student theses avoids violations of my personal copyright.

Leobersdorf, in October 2024

---

Signature

# Acknowledgements

I would like to take this opportunity to thank my supervisor Univ.Prof. Mag. Dr. Yury Vetyukov for his unique commitment. I thoroughly enjoyed our discussions about mechanical-mathematical problems and I was able to learn a lot from you. I would also like to thank you for the opportunity to collaborate on a publication and a conference contribution. The book chapter on parametrically excited beams published in Progress in Continuum Mechanics [1], as well as the opportunity to incorporate the findings of this thesis into a contribution for the ASCE Engineering Mechanics Institute 2024 International Conference, are a great sign of appreciation and increased my interest in mechanics even more.

Furthermore, I want to thank all my fellow students for the mutual support since the beginning of my studies. Especially, I would like to mention my colleagues Stefan Kinzelberger, Daniel Patauner and Mario Wedl. I will always remember studying together into the night, motivating each other during stressful periods, but especially the fun times we had.

Above all, I would like to thank my parents Michaela and Roman for making it possible for me to go to university. Without your support and guidance through all the ups and downs, this study would have been unthinkable. I would also like to thank my girlfriend Katharina for her enormous support and for proofreading my thesis.

# Abstract

In elastic systems, small changes in stiffness or inertia yield a shift in natural frequencies. The so-called energy approach allows to obtain a linear approximation to estimate this frequency shift using energetic considerations. The goal of this thesis is to test this energy approach for a square plate with a crack or applied mass for different mode shapes. In particular, the behaviour of the frequency shift is to be determined with finite element analyses and checked for convergence with the solution according to the energy approach.

First, necessary theoretical aspects from Kirchhoff's plate theory and the linear finite element method are stated. Then, the energy approach is introduced and a mathematical justification is given. Afterwards, the simulation model and the used meshes are presented. Following this, the results of the finite element analyses for the plate with additional mass/crack are discussed.

The simulations clearly show that the previously known form of the energy approach fails in the case of repeated natural frequencies, as they occur with square plates. Apart from that, good correspondence can be seen for the considered examples.

# Kurzfassung

In elastischen Systemen äußern sich geringfügige Änderungen der Steifigkeit oder Massenträgheit in einer Verschiebung der Eigenfrequenzen. Das sogenannte Energieverfahren ermöglicht es, mit Hilfe von energetischen Betrachtungen eine lineare Approximation zu bestimmen, mit welcher die Frequenzverschiebung abgeschätzt werden kann. Das Ziel der vorliegenden Arbeit ist es, dieses Energieverfahren für eine quadratische Platte mit Riss oder aufgebracht Masse für verschiedene Eigenmoden zu prüfen. Speziell soll dabei der Verlauf der Frequenzverschiebung durch Finite-Elemente-Analysen ermittelt und auf Konvergenz mit der linearen Näherungslösung untersucht werden.

Zunächst werden erforderliche theoretische Zusammenhänge aus der Kirchhoffschen Plattentheorie und der linearen Finite-Elemente-Methode angeführt. Ebenso wird das Energieverfahren erläutert und durch eine Herleitung gestützt. Anschließend wird das Simulationsmodell und die verwendeten Netze vorgestellt. Darauf folgend werden die Ergebnisse der Finite-Elemente-Analysen für die Platte mit Zusatzmasse/Riss diskutiert.

Die Simulationen zeigen deutlich, dass das Energieverfahren in der bisher bekannten Form bei mehrfachen Eigenfrequenzen, wie sie bei quadratischen Platten auftreten, scheitert. Abgesehen davon lässt sich bei den betrachteten Problemen eine gute Übereinstimmung feststellen.

# Contents

<b>1</b>	<b>Introduction</b>	<b>1</b>
<b>2</b>	<b>Theoretical Background</b>	<b>3</b>
2.1	Kirchhoff's plate theory . . . . .	3
2.1.1	Plane stress state . . . . .	4
2.1.2	Kinematics and strain energy in a plate problem . . . . .	6
2.1.3	Equilibrium conditions and plate equation . . . . .	9
2.1.4	Free vibration analysis . . . . .	11
2.2	Linear Finite Element Method . . . . .	12
2.2.1	General formulation in continuum mechanics . . . . .	12
2.2.2	Approach of this thesis for the plate problem . . . . .	16
2.2.3	Local shape functions and numerical integration . . . . .	16
2.3	Energy approach to estimate changes in the natural frequencies . . . . .	20
<b>3</b>	<b>Finite Element Model</b>	<b>23</b>
3.1	Bogner-Fox-Schmit element formulation . . . . .	23
3.2	Rectangular mesh . . . . .	26
3.3	Skewed mesh . . . . .	28
3.3.1	The problem with the $\mathcal{C}^1$ -continuity . . . . .	28
3.3.2	Double mapping – achieving $\mathcal{C}^1$ -continuity . . . . .	30
3.3.3	Eigenvalue problem . . . . .	32
3.4	Mesh convergence study . . . . .	32
<b>4</b>	<b>Plate with added line mass</b>	<b>35</b>
4.1	Centric line mass . . . . .	35
4.2	Skewed line mass . . . . .	39
<b>5</b>	<b>Cracked plate</b>	<b>42</b>
5.1	Crack implementation and adapted energy approach . . . . .	42

5.2	Centric crack . . . . .	44
5.2.1	Potential of the spring and complementary energy . . . . .	44
5.2.2	Testing the cracked finite element model . . . . .	45
5.2.3	Comparison of reference solution and energy approach . . . . .	46
5.3	Skewed crack . . . . .	49
5.3.1	Potential of the spring and complementary energy . . . . .	50
5.3.2	Comparison of reference solution and energy approach . . . . .	51
<b>6</b>	<b>Conclusion and Outlook</b>	<b>54</b>

# 1 Introduction

An interesting question occurs when investigating the natural vibrations of an elastic structure (modal analysis): how do small changes in inertial or stiffness properties affect the spectrum of natural frequencies? It is well known that local damage due to a crack or changed inertia from an applied mass result in lower natural frequencies of the system. If the behaviour of the origin system is already studied, is it even necessary to execute another whole modal analysis for the perturbed system? No, there exists a linear approximation for the change in natural frequencies of the perturbed system based on the so-called energy approach. The energy approach allows a quick calculation of the frequency shifts (difference between natural frequency of perturbed and unperturbed system) when the vibration modes of the unperturbed system are known.

In the 13<sup>th</sup> International Symposium on Vibrations of Continuous Systems, which took place in Canada in 2023 [15], the energy approach for natural frequencies of a simply supported rectangular plate with cracks was presented and tested with different dimensions of the crack and the plate itself. The energy approach was treated analytically in this conference contribution, which is possible for such simple boundary conditions of the plate. This awakened motivation to examine the energy approach further for plates with more complex boundary conditions, where the natural vibrations cannot be described by simple analytical expressions. As a result, the prediction according to the energy approach has to be obtained by the finite element method. In particular, the energy approach formula is further investigated for plate problems with cracks and also with added masses. The goal is to determine the behaviour of the frequency shift in a clamped square plate due to applied masses or cracks in dependence on the measure of the structural change and to compare the predictions obtained by the energy approach to the results of the conventional approach, which requires re-meshing in dependence on the geometry of the structural change and solving a new eigenvalue problem. The main question is if the initial slopes of these two solutions (reference solution and energy method) approach each other for small property changes in different mode shapes. For

this sake, a finite element model using Bogner-Fox-Schmit elements [19] was developed in Wolfram Mathematica [22].

An interesting fact is that there is also a practical demand for such efficient prediction methods for the non-destructive inspection of elastic systems using frequency measurements (e.g. for plate-like structures in machine coverings or casings) [11]. Changes in natural frequencies of structures are highly dependent on the location and size of damage and therefore used to detect and characterise it [11].

In Chapter 2 of this thesis some theoretical aspects about Kirchhoff's plate theory and the linear finite element method are given. At the end of Chapter 2 the mentioned energy approach is introduced and a mathematical justification is presented for the case of unchanged kinematics (admissible deformations of unperturbed and perturbed system are the same). Chapter 3 deals with the implemented finite element model and discusses the used rectangular and skewed mesh. Following this, in Chapter 4, the energy approach is tested and compared to the reference solution in the case of a plate with applied line mass (centric and skewed). In Chapter 5 the cracked plate is discussed. First, the used crack implementation is given, then the energy approach is tested and compared again to the reference solution (centric and skewed). Finally, Chapter 6 summarizes the findings of this thesis and provides an outlook of possible further investigations around this topic.

# 2 Theoretical Background

## 2.1 Kirchhoff's plate theory

First of all, we need to distinguish between curved and planar thin-walled surface-like structures. Curved structures are called *shells* while the planar ones are separated into *disks* and *plates*. Disks are only loaded within its plane, while structures with perpendicular loading states are called plates. Structures can be seen as thin-walled if the thickness is much smaller compared to the other dimensions (or a characteristic length). In this thesis, the vibrations of a thin-walled square plate clamped at all four edges are simulated with the account for added masses and cracks. This section should give an overview of the used mechanical theory to describe plate problems mathematically. For thin-walled plates an analogous theory to the Bernoulli-Euler beam was formulated by Kirchhoff<sup>1</sup>.

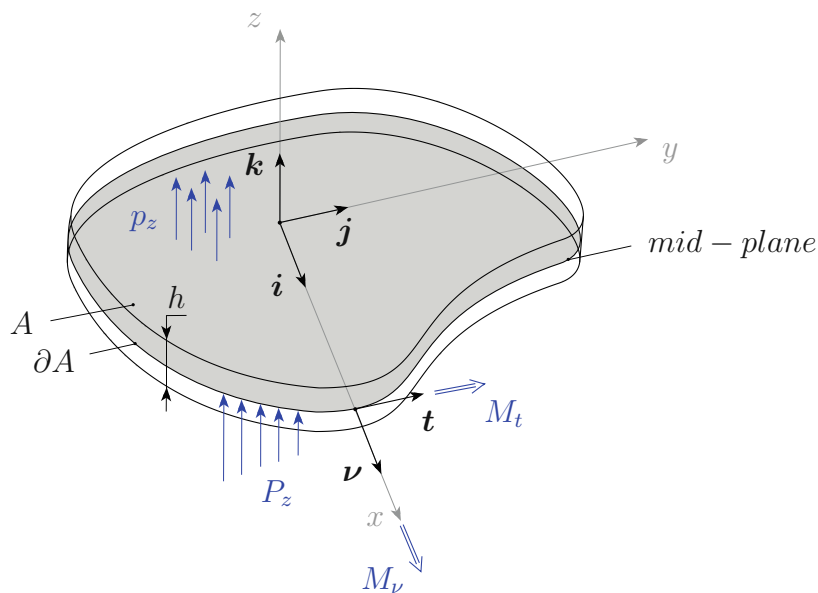


Figure 2.1: Sketch of a plate problem

<sup>1</sup>Gustav Robert Kirchhoff, 1824-1887, German physicist [16]

This plate theory is based on a several assumptions [4, 16, 21]:

- As already mentioned, the thickness is small compared to the other dimensions.
- Equations are formulated for the mid-plane of the plate (see Figure 2.1).
- Kirchhoff's hypothesis is valid, which means that normals to the undeformed mid-surface stay perpendicular to the deformed mid-plane  $\rightarrow$  shear rigid plate.
- The distance between points along the normals to the mid-plane remains the same. According to this assumption a plane strain would occur because  $\varepsilon_z = 0$ . In the next assumption, a plane stress state is assumed - here a contradiction of Kirchhoff's plate theory should be pointed out.
- A plane stress is assumed. Therefore the stresses  $\sigma_z, \tau_{xz}$  and  $\tau_{yz}$  are zero. As a consequence the strain component perpendicular to the plate  $\varepsilon_z$  will be different from zero.
- Geometric linearity - small deformation compared to the dimension of the plate and small strains are considered.
- Linear elastic material behaviour - Hooke's law is valid. Furthermore isotropic homogeneous plates are treated.

In these assumptions one can notice that Kirchhoff's plate theory is not free of contradictions. However, practical experience shows that the resulting errors are negligible if the plate thickness is sufficiently small [16].

### 2.1.1 Plane stress state

As shown in Figure 2.1, a three dimensional  $\mathbf{i}-\mathbf{j}-\mathbf{k}$  coordinate system with a  $\mathbf{k}$ -axis perpendicular to the mid-plane is used. In this thesis dyadic products like  $\mathbf{i}\mathbf{i}$  are written without the often used symbol  $\otimes$ . With this notation the three dimensional stress tensor  $\boldsymbol{\sigma}_3$  can be expressed in general as [21]

$$\boldsymbol{\sigma}_3 = \boldsymbol{\sigma} + \boldsymbol{\tau}\mathbf{k} + \mathbf{k}\boldsymbol{\tau} + \sigma_z\mathbf{k}\mathbf{k}, \quad (2.1)$$

where  $\boldsymbol{\sigma} = \sigma_x\mathbf{i}\mathbf{i} + \sigma_y\mathbf{j}\mathbf{j} + \tau_{xy}(\mathbf{i}\mathbf{j} + \mathbf{j}\mathbf{i})$  represents the plane stress tensor and  $\boldsymbol{\tau} = \tau_{xz}\mathbf{i} + \tau_{yz}\mathbf{j}$  denotes the shear stress vector. Using Kirchhoff's assumptions of the plate theory the stress tensor  $\boldsymbol{\sigma}_3$  simplifies to  $\boldsymbol{\sigma}_3 = \boldsymbol{\sigma}$ , which is the considered plane stress state. Note

that the assumption that shear stresses  $\boldsymbol{\tau}$  equal to zero  $\boldsymbol{\tau} = \mathbf{0}$  for plate problems (perpendicular loading states) cannot be true. They have to counteract the transverse load, which reveals another inconsistency of this plate theory. However, it is still possible to calculate so-called statically equivalent estimates for the shear stresses  $\tau_{xz}, \tau_{yz}$  by using the stress resultants [4].

The three dimensional linear strain tensor can be formulated in the same way [21]:

$$\boldsymbol{\varepsilon}_3 = \boldsymbol{\varepsilon}_\perp + \boldsymbol{\gamma}\mathbf{k} + \mathbf{k}\boldsymbol{\gamma} + \varepsilon_z\mathbf{k}\mathbf{k}. \quad (2.2)$$

Here  $\boldsymbol{\varepsilon}_\perp = \varepsilon_x\mathbf{i}\mathbf{i} + \varepsilon_y\mathbf{j}\mathbf{j} + \gamma_{xy}(\mathbf{i}\mathbf{j} + \mathbf{j}\mathbf{i})$  indicates the planar strain tensor and  $\boldsymbol{\gamma} = \gamma_{xz}\mathbf{i} + \gamma_{yz}\mathbf{j}$  is used for the shear strain vector. The constitutive law for an ideal elastic and isotropic body (Hooke's law) is given by [13]:

$$\boldsymbol{\varepsilon}_3 = \frac{1+\nu}{E}\boldsymbol{\sigma}_3 - \frac{\nu}{E}\mathbf{I}\operatorname{tr}\boldsymbol{\sigma}_3 \quad \text{and} \quad \operatorname{tr}\boldsymbol{\varepsilon}_3 = \frac{1-2\nu}{E}\operatorname{tr}\boldsymbol{\sigma}_3, \quad (2.3a)$$

$$\boldsymbol{\sigma}_3 = \frac{E}{1+\nu}\boldsymbol{\varepsilon}_3 + \frac{E\nu}{(1-2\nu)(1+\nu)}\mathbf{I}\operatorname{tr}\boldsymbol{\varepsilon}_3 \quad \text{and} \quad \operatorname{tr}\boldsymbol{\sigma}_3 = \frac{E}{1-2\nu}\operatorname{tr}\boldsymbol{\varepsilon}_3. \quad (2.3b)$$

In Equation (2.3) the Young's modulus is denoted with  $E$ , the Poisson's ratio is  $\nu$ , the trace operator is symbolized with  $\operatorname{tr}$  and for the three dimensional unit tensor  $\mathbf{I}$  is used. In the next step a fomulation of Hooke's law for a plane stress state like in Equation (2.3b) is derived. If the expressions for  $\boldsymbol{\varepsilon}_3$  in Equations (2.3a) and (2.2) are set equal and the unit tensor  $\mathbf{I}$  is written as  $\mathbf{I} = \mathbf{I}_\perp + \mathbf{k}\mathbf{k}$ , one gets [21]

$$\boldsymbol{\varepsilon}_3 = \boldsymbol{\varepsilon}_\perp + \boldsymbol{\gamma}\mathbf{k} + \mathbf{k}\boldsymbol{\gamma} + \varepsilon_z\mathbf{k}\mathbf{k} = \frac{1+\nu}{E}\boldsymbol{\sigma} - \frac{\nu}{E}(\mathbf{I}_\perp + \mathbf{k}\mathbf{k})\operatorname{tr}\boldsymbol{\sigma}. \quad (2.4)$$

As a result the shear strain vector  $\boldsymbol{\gamma}$  must disappear. By comparing the  $\mathbf{k}\mathbf{k}$ -components one can see that  $\varepsilon_z$  does not become zero. The transversal strain component becomes equal to

$$\varepsilon_z = -\frac{\nu}{E}\operatorname{tr}\boldsymbol{\sigma}, \quad (2.5)$$

where a short look at the made assumptions points out the mentioned contradiction in this plate theory. Now the planar strain tensor is expressed by

$$\boldsymbol{\varepsilon}_\perp = \frac{1+\nu}{E}\boldsymbol{\sigma} - \frac{\nu}{E}\mathbf{I}_\perp\operatorname{tr}\boldsymbol{\sigma}. \quad (2.6)$$

Further relations in this section and in the following two sections refer closely to [21].

To obtain an expression for  $\text{tr } \boldsymbol{\sigma}$  the trace operator is applied on Equation (2.6)

$$\text{tr } \boldsymbol{\varepsilon}_\perp = \frac{1 + \nu}{E} \text{tr } \boldsymbol{\sigma} - \frac{\nu}{E} 2 \text{tr } \boldsymbol{\sigma}, \quad (2.7)$$

where  $\text{tr } \boldsymbol{\sigma}$  is easily determined as

$$\text{tr } \boldsymbol{\sigma} = \frac{E}{1 - \nu} \text{tr } \boldsymbol{\varepsilon}_\perp. \quad (2.8)$$

Using the expression for  $\text{tr } \boldsymbol{\sigma}$  and Equation (2.6), a final formulation for  $\boldsymbol{\sigma}(\boldsymbol{\varepsilon}_\perp)$  is given by

$$\boldsymbol{\sigma} = \frac{E}{1 + \nu} \boldsymbol{\varepsilon}_\perp + \frac{E\nu}{(1 + \nu)(1 - \nu)} \mathbf{I}_\perp \text{tr } \boldsymbol{\varepsilon}_\perp, \quad (2.9)$$

or in a shorter version with  $Y = E(1 - \nu^2)^{-1}$  as

$$\boldsymbol{\sigma} = Y\nu \mathbf{I}_\perp \text{tr } \boldsymbol{\varepsilon}_\perp + Y(1 - \nu) \boldsymbol{\varepsilon}_\perp. \quad (2.10)$$

### 2.1.2 Kinematics and strain energy in a plate problem

The position vector of a point  $P$  within the plate (see Figure 2.2) is described with its normal projection point  $P_0$  on the undeformed mid-plane by

$$\mathbf{R}_3 = \mathbf{R}_0 + z\mathbf{k}. \quad (2.11)$$

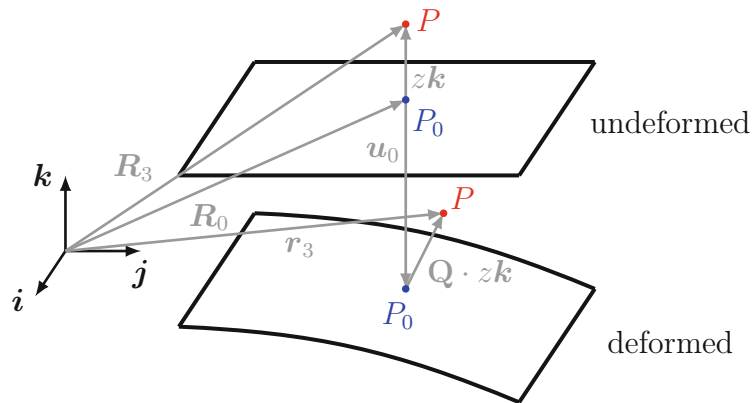


Figure 2.2: Kinematic assumptions for the plate problem

In the current or deformed configuration, the position vector becomes

$$\mathbf{r}_3 = \mathbf{R}_0 + \mathbf{u}_0 + \mathbf{Q} \cdot z\mathbf{k}, \quad (2.12)$$

where  $\mathbf{u}_0$  describes the displacement vector of point  $P_0$  and  $\mathbf{Q}$  represents an orthogonal rotation tensor. The rotation tensor  $\mathbf{Q}$  within the considered geometrically linear theory can be formulated as  $\mathbf{Q} = \mathbf{I}_3 + \boldsymbol{\omega} \times \mathbf{I}_3 + \mathcal{O}(\boldsymbol{\omega}^2)$  with an axial vector  $\boldsymbol{\omega}$ . For the displacement vector of point  $P$  one gets

$$\mathbf{u}_3 = \mathbf{r}_3 - \mathbf{R}_3 = \mathbf{u}_0 + z(\mathbf{Q} - \mathbf{I}_3) \cdot \mathbf{k} = \mathbf{u}_0 + z(\boldsymbol{\omega} \times \mathbf{I}_3) \cdot \mathbf{k} = \mathbf{u}_0 + z\boldsymbol{\omega} \times \mathbf{k}. \quad (2.13)$$

Here, it is clear that the  $z$ -component of  $\boldsymbol{\omega}$  has no influence on the displacement vector, so it is considered as zero without any effects - hence  $\boldsymbol{\omega}$  is a planar vector within the plate surface. If the cross product  $\boldsymbol{\omega} \times \mathbf{k}$  is denoted as  $\boldsymbol{\psi}$  and the nabla-operator in the three dimensional space  $\nabla_3 = \nabla + \mathbf{k}\partial_z$  expressed by using a planar part  $\nabla$ , the deformation gradient becomes equal to

$$\nabla_3 \mathbf{u}_3 = \nabla \mathbf{u}_0 + z\nabla \boldsymbol{\psi} + \mathbf{k}\boldsymbol{\psi}. \quad (2.14)$$

Furthermore, the displacement vector  $\mathbf{u}_0$  of a point  $P_0$  in the mid-plane can generally be split into a part within the plane (for disk problems) and another part normal to the plane, which is considered here for the plate problems. This perpendicular part is called the deflection of the mid-plane and is given by  $w = \mathbf{u}_0 \cdot \mathbf{k}$ . Because in the plate bending problem we focus only on the transversal displacement we can set  $\mathbf{u}_0 = w\mathbf{k}$  and do not need to consider the in-plane part. Referring to the assumptions mentioned at the beginning, zero strain in the direction of the thickness of the plate is assumed. If one scalar multiplies  $\mathbf{u}_3 \cdot \mathbf{k}$ , it can be easily seen that this equals  $w$ , as a result no strain component  $\varepsilon_z$  will be obtained. In the geometrically linear theory the three dimensional strain tensor  $\boldsymbol{\varepsilon}_3$  is given by the symmetrical part of the deformation gradient [2]

$$\boldsymbol{\varepsilon}_3 = (\nabla_3 \mathbf{u}_3)^S = \frac{1}{2} [(\nabla_3 \mathbf{u}_3)^T + (\nabla_3 \mathbf{u}_3)]. \quad (2.15)$$

Using  $\mathbf{u}_0 = w\mathbf{k}$  into (2.15) yields the following expression:

$$\boldsymbol{\varepsilon}_3 = -z\boldsymbol{\kappa} + (\mathbf{k}\boldsymbol{\gamma})^S. \quad (2.16)$$

Here  $\boldsymbol{\kappa} = -(\nabla \boldsymbol{\psi})^S$  is the linearised curvature tensor and  $\boldsymbol{\gamma} = \nabla w + \boldsymbol{\psi}$  represents the shear strain vector, which was introduced earlier. In the last step to obtain an expression for the planar strain tensor  $\boldsymbol{\varepsilon}_\perp$ , which is necessary for (2.10), Kirchoff's assumption of a shear rigid plate must be taken into account. The shear strain vector becomes zero

$\boldsymbol{\gamma} = \nabla w + \boldsymbol{\psi} = \mathbf{0}$ , so normals to the mid-plane remain normal. As a result, we write that  $\boldsymbol{\psi} = -\nabla w$  which leads to  $\boldsymbol{\kappa} = -(\nabla \boldsymbol{\psi})^S = \nabla \nabla w$ . Hence, the strain tensor becomes equal to

$$\boldsymbol{\varepsilon}_3 = -z \boldsymbol{\kappa} = -z \nabla \nabla w \equiv \boldsymbol{\varepsilon}_\perp. \quad (2.17)$$

Now, further required quantities as the tensor of moments, the plate stiffness and the strain energy are derived. At first, the internal virtual work reads as

$$\delta A_i = - \int_V \boldsymbol{\sigma} \cdot \cdot \delta \boldsymbol{\varepsilon}_\perp dV = - \int_A \left( - \int_h \boldsymbol{\sigma} z dz \cdot \cdot \delta \boldsymbol{\kappa} \right) dA = - \int_A \boldsymbol{m} \cdot \cdot \delta \boldsymbol{\kappa} dA, \quad (2.18)$$

where  $\boldsymbol{m}$  is the tensor of moments. The calculation of  $\boldsymbol{m}$  is done by inserting the planar strain tensor (2.17) into the constitutive law (2.10)

$$\boldsymbol{\sigma} = Y \nu \mathbf{I}_\perp (-z \operatorname{tr} \boldsymbol{\kappa}) + Y(1 - \nu)(-z \boldsymbol{\kappa}) \quad (2.19)$$

and integrating over the plate thickness with a symmetric interval  $[-h/2, h/2]$ :

$$\boldsymbol{m} = - \int_{-h/2}^{h/2} [Y \nu \mathbf{I}_\perp z (-z \operatorname{tr} \boldsymbol{\kappa}) + Y(1 - \nu) z (-z \boldsymbol{\kappa})] dz, \quad (2.20)$$

or in a shorter version

$$\boldsymbol{m} = D \nu \mathbf{I}_\perp \operatorname{tr} \boldsymbol{\kappa} + D(1 - \nu) \boldsymbol{\kappa}. \quad (2.21)$$

Here,  $D$  is used for the so-called plate stiffness (flexural rigidity):

$$D = \int_{-h/2}^{h/2} Y z^2 dz = \frac{Y h^3}{12} = \frac{E h^3}{12(1 + \nu)(1 - \nu)} = \frac{E h^3}{12(1 - \nu^2)}. \quad (2.22)$$

Furthermore, the bending strain energy density per unit area  $u_b$  is expressed by

$$u_b = \frac{1}{2} D [\nu (\operatorname{tr} \boldsymbol{\kappa})^2 + (1 - \nu) \boldsymbol{\kappa} \cdot \cdot \boldsymbol{\kappa}] \quad \text{or} \quad u_b = \frac{1}{2} \boldsymbol{m} \cdot \cdot \boldsymbol{\kappa}. \quad (2.23)$$

To get the total bending strain energy  $U_b$  we have to integrate  $u_b$  over the area of the plate:

$$U_b = \int_A u_b dA = \frac{1}{2} \int_A \boldsymbol{m} \cdot \cdot \boldsymbol{\kappa} dA. \quad (2.24)$$

### 2.1.3 Equilibrium conditions and plate equation

In this section, the equilibrium conditions for the plate problem are derived, which are necessary for the final plate equation. We start with the principle of virtual work  $\delta A_e + \delta A_i = 0$ , where the total of the virtual external and internal work is zero for an equilibrium state. The internal work  $\delta A_i$  has already been expressed in Equation (2.18). Using the linearised curvature tensor  $\boldsymbol{\kappa} = \nabla \nabla w$  we write

$$\begin{aligned} \delta A_i &= - \int_A \mathbf{m} \cdot \cdot \delta \boldsymbol{\kappa} \, dA = - \int_A \mathbf{m} \cdot \cdot \delta \nabla \nabla w \, dA \\ &= \int_A (\nabla \cdot \mathbf{m}) \cdot \delta(\nabla w) \, dA - \oint_{\partial A} \boldsymbol{\nu} \cdot \mathbf{m} \cdot \delta \nabla w \, ds \\ &= - \int_A (\nabla \cdot \nabla \cdot \mathbf{m}) \delta w \, dA + \oint_{\partial A} (\nabla \cdot \mathbf{m}) \cdot \boldsymbol{\nu} \delta w \, ds - \oint_{\partial A} \boldsymbol{\nu} \cdot \mathbf{m} \cdot \delta \nabla w \, ds, \end{aligned} \quad (2.25)$$

where  $\boldsymbol{\nu}$  is the unit normal vector to the boundary  $\partial A$  of the plate area  $A$ , see Figure 2.1. Next, the virtual work of external forces is given by

$$\delta A_e = \int_A p_z \delta w \, dA + \oint_{\partial A} (P_z \delta w + \mathbf{M} \cdot \delta \boldsymbol{\omega}) \, ds. \quad (2.26)$$

Here, the moment vector  $\mathbf{M}$  performs virtual work on the virtual rotations  $\delta \boldsymbol{\omega} = \mathbf{k} \times \delta \boldsymbol{\psi}$ . Using  $\delta \boldsymbol{\psi} = -\delta \nabla w$  we further write  $\mathbf{M} \cdot \delta \boldsymbol{\omega} = \mathbf{M} \cdot \mathbf{k} \times \delta \boldsymbol{\psi} = \mathbf{M} \times \mathbf{k} \cdot \delta \nabla w$ . Subsequently the principle of virtual work for the plate reads

$$0 = \int_A (p_z - \nabla \cdot \nabla \cdot \mathbf{m}) \delta w \, dA + \oint_{\partial A} [P_z + (\nabla \cdot \mathbf{m}) \cdot \boldsymbol{\nu}] \delta w \, ds - \oint_{\partial A} (\boldsymbol{\nu} \cdot \mathbf{m} + \mathbf{M} \times \mathbf{k}) \cdot \delta \nabla w \, ds. \quad (2.27)$$

In Equation (2.27) we see that not all virtual displacements can be chosen independently. The variation of the deflection gradient  $\delta \nabla w$  cannot be chosen arbitrarily, therefore this term must be examined in more detail. This gradient is given by

$$\nabla w = \boldsymbol{\nu} (\boldsymbol{\nu} \cdot \nabla w) + \mathbf{t} (\mathbf{t} \cdot \nabla w) = \boldsymbol{\nu} \frac{\partial w}{\partial \nu} + \mathbf{t} \frac{\partial w}{\partial s}, \quad (2.28)$$

where  $\partial_\nu = \partial(\cdot)/\partial \nu$  and  $\partial_s = \partial(\cdot)/\partial s$  are the directional derivatives,  $\mathbf{t}$  represents the unit vector tangential to the boundary  $\partial A$  of area  $A$ . Especially  $\partial_\nu w$  represents the inclination of the plate at the borderline. By the use of the commutativity  $\delta \nabla w = \nabla \delta w$ ,

the last term of Equation (2.27) becomes equal to

$$\begin{aligned}
 & - \oint_{\partial A} (\boldsymbol{\nu} \cdot \mathbf{m} + \mathbf{M} \times \mathbf{k}) \cdot \delta \nabla w \, ds = \\
 & = - \oint_{\partial A} (\boldsymbol{\nu} \cdot \mathbf{m} \cdot \boldsymbol{\nu} + \mathbf{M} \times \mathbf{k} \cdot \boldsymbol{\nu}) \delta \partial_\nu w \, ds - \oint_{\partial A} (\boldsymbol{\nu} \cdot \mathbf{m} \cdot \mathbf{t} + \mathbf{M} \times \mathbf{k} \cdot \mathbf{t}) \partial_s \delta w \, ds \\
 & = - \oint_{\partial A} (\boldsymbol{\nu} \cdot \mathbf{m} \cdot \boldsymbol{\nu} + \mathbf{M} \times \mathbf{k} \cdot \boldsymbol{\nu}) \delta \partial_\nu w \, ds + \oint_{\partial A} \partial_s (\boldsymbol{\nu} \cdot \mathbf{m} \cdot \mathbf{t} + \mathbf{M} \times \mathbf{k} \cdot \mathbf{t}) \delta w \, ds.
 \end{aligned} \tag{2.29}$$

In Equation (2.29) the integral with  $(\dots) \partial_s \delta w$  was rewritten using the integration by parts. No boundary terms arise because of the closed path of the line integral. The cross products with  $\mathbf{M}$  result in a bending moment  $M_t$  around an axis with direction  $\mathbf{t}$  and analogous into a twisting moment  $M_\nu$  around an axis with direction  $\boldsymbol{\nu}$ :

$$\begin{aligned}
 \mathbf{M} \times \mathbf{k} \cdot \boldsymbol{\nu} &= \mathbf{k} \times \boldsymbol{\nu} \cdot \mathbf{M} = \mathbf{t} \cdot \mathbf{M} = M_t, \\
 \mathbf{M} \times \mathbf{k} \cdot \mathbf{t} &= \mathbf{k} \times \mathbf{t} \cdot \mathbf{M} = -\boldsymbol{\nu} \cdot \mathbf{M} = -M_\nu.
 \end{aligned} \tag{2.30}$$

Finally, the principle of virtual work for the plate reads

$$\begin{aligned}
 0 &= \int_A (p_z - \nabla \cdot \nabla \cdot \mathbf{m}) \delta w \, dA - \oint_{\partial A} (\boldsymbol{\nu} \cdot \mathbf{m} \cdot \boldsymbol{\nu} + M_t) \delta \partial_\nu w \, ds \\
 &+ \oint_{\partial A} [P_z + (\nabla \cdot \mathbf{m}) \cdot \boldsymbol{\nu} + \partial_s (\boldsymbol{\nu} \cdot \mathbf{m} \cdot \mathbf{t}) - \partial_s M_\nu] \delta w \, ds.
 \end{aligned} \tag{2.31}$$

The occurring variations  $\delta w$  and  $\delta \partial_\nu w$  can be chosen arbitrarily, therefore the terms in brackets must vanish. This yields the sought for equilibrium conditions with  $\mathbf{q} = -\nabla \cdot \mathbf{m}$ :

$$\begin{aligned}
 A: \quad \nabla \cdot \mathbf{q} + p_z &= 0, \\
 \partial A: \quad \mathbf{q} \cdot \boldsymbol{\nu} - \partial_s (\boldsymbol{\nu} \cdot \mathbf{m} \cdot \mathbf{t}) &= P_z - \partial_s M_\nu.
 \end{aligned} \tag{2.32}$$

Using  $\nabla \cdot \mathbf{q} + p_z = 0$ , the Laplace operator  $\Delta = \nabla \cdot \nabla = \nabla^2$  and the following relations:

$$\begin{aligned}
 \nabla \cdot \boldsymbol{\kappa} &= \nabla \cdot \nabla (\nabla w) = \Delta (\nabla w) = \nabla (\Delta w), \quad \text{tr} \boldsymbol{\kappa} = \text{tr} (\nabla \nabla w) = \nabla \cdot \nabla w = \Delta w, \\
 \mathbf{q} &= -\nabla \cdot \mathbf{m} = -D \nu \nabla \text{tr} \boldsymbol{\kappa} - D(1 - \nu) \nabla \cdot \boldsymbol{\kappa} = -D \nabla (\Delta w),
 \end{aligned} \tag{2.33}$$

one obtains the fourth-order plate equation for an isotropic shear-rigid plate according to Kirchhoff:

$$D \Delta \Delta w = p_z. \tag{2.34}$$

### 2.1.4 Free vibration analysis

This section covers the solution for natural vibrations of plates. At first the fourth-order plate equation (2.34) is adapted for the dynamical analysis. Using  $p_z = 0$  and adding a dynamical term  $-\rho h \ddot{w}$  (inertial force, also called d'Alembert force with  $\rho h$  being mass per unit area) on the right side of the equation, one gets

$$D \nabla \nabla w(x, y, t) = -\rho h \ddot{w}(x, y, t). \quad (2.35)$$

Natural vibrations are now studied by separating the time  $t$  and position  $(x, y)$  variables. According to [3] the following separation ansatz is suitable:

$$w(x, y, t) = W(x, y)T(t). \quad (2.36)$$

This ansatz inserted into the partial differential equation (2.35) leads to

$$\frac{D \nabla \nabla W(x, y)}{\rho h W(x, y)} = -\frac{\ddot{T}(t)}{T(t)} \stackrel{!}{=} \omega^2. \quad (2.37)$$

To ensure that both sides  $W(x, y)$  and  $T(t)$  of Equation (2.37) are equal for any time  $t$  or position  $(x, y)$ , they have to be constant. The constant is chosen as  $\omega^2$ , which is the squared natural frequency [3]. As a result, one gets two separate equations:

$$\begin{aligned} \nabla \nabla W(x, y) - \frac{\rho h \omega^2}{D} W(x, y) &= 0, \\ \ddot{T}(t) + \omega^2 T(t) &= 0. \end{aligned} \quad (2.38)$$

The solution for the time function  $T(t)$  is expressed as  $T(t) = \sin(\omega t + \varphi)$  or using the imaginary unit as  $T(t) = e^{i(\omega t + \varphi)}$ . In the next step, the remaining eigenvalue problem in (2.38) for the mode shapes  $W(x, y)$  and natural frequencies  $\omega$  can be solved. This succeeds analytically only in a few simple cases, for example the simply supported rectangular ( $l_1 \times l_2$ ) plate. In this certain problem Navier's method with the ansatz

$$W(x, y) = \sum_{n=1}^N \sum_{m=1}^M W_{mn} \sin\left(\frac{m\pi}{l_1}x\right) \sin\left(\frac{n\pi}{l_2}y\right), \quad (2.39)$$

leads to the goal; see also [4] for the solution of the static deflection  $W(x, y)$  under a certain load and [3] for the eigenvalue problem. In general, for an eigenvalue problem

of plates with arbitrary boundary conditions, one needs to make use of approximate solution techniques like Ritz, Galerkin or numerical methods like the finite element method. At this point, the paper from A. W. Leissa should also be mentioned [14]. Leissa gives an overview of all 21 possible combinations of boundary conditions for a rectangular plate and determines the natural vibrations. Six of them can be determined analytically exact. For the remaining problems including the square clamped plate (considered in this thesis) Ritz's method was used. We, however, do not use this analytical technique as we need finite elements for more complicated problems anyways.

## 2.2 Linear Finite Element Method

Linear finite element analyses are widely used and one could say became daily business in the academic research and mechanical engineering nowadays. Problems in continuum mechanics lead to partial differential equations, which can only be solved analytically in a few simple cases [10]. The linear finite element method (a numerical method) is used to obtain numerical solutions when analytical solutions can not be found in general or determined in a reasonable amount of time. Moreover, it is worth mentioning that the whole process of simulating a problem using the finite element method (FEM) is called finite element analysis (FEA). As in Section 2.1.4 already mentioned, the calculation of eigenmodes and eigenvalues from Equation (2.38) succeeds analytically only in a few simple ways. Therefore the linear finite element method is used for the eigenvalue problem of the clamped square plate with added masses or cracks which is treated in this thesis. Due to this, some basics of the linear FEM are discussed in this section.

At first some assumptions are made in the linear finite element method [18]:

- Small deformations, small displacement gradients and small strains - the Green Lagrange strain tensor corresponds to the linear strain tensor:  $\mathbf{G} \approx \boldsymbol{\varepsilon}_3$
- No material nonlinearities, contact or bifurcation of equilibria
- Equilibrium conditions are formulated for the undeformed system

### 2.2.1 General formulation in continuum mechanics

Before the finite element method can be applied, one has to transfer the strong formulation of a problem (partial differential equations) into the so-called weak formulation (integral form derived with calculus of variation e.g. principle of virtual work). This two

formulations are mathematically equivalent [20]. The weak formulation is the starting point for the finite element method. If an arbitrary elastic body with surface area  $O$ , volume  $V$  and some kinematic boundary conditions is considered, the principle of virtual work (global equilibrium condition) reads as [18]

$$\delta A_i + \delta A_e = - \int_V \boldsymbol{\sigma}_3 \cdot \cdot \delta \boldsymbol{\varepsilon}_3 dV + \int_O \mathbf{t} \cdot \delta \mathbf{u}_O dO + \int_V \mathbf{k}_V \cdot \delta \mathbf{u} dV = 0, \quad (2.40)$$

where  $\mathbf{t}$  is used for surface loads (traction forces),  $\mathbf{k}_V$  are volume loads and  $\mathbf{u} = \mathbf{u}(x, y, z)$  is the displacement of a material point  $P$ . To get an approximate solution for primarily the displacement field  $\mathbf{u}$  (displacement driven finite element method) a special form of Ritz's method is used. The system is discretized with a lot of fixed points (nodes) all over the volume  $V$  and surface  $O$ . Connecting those points with lines delivers a mesh and divides the considered body into many small sub-volumes with nodes on the edges. This are the so-called finite elements, sketched in Figure 2.3.

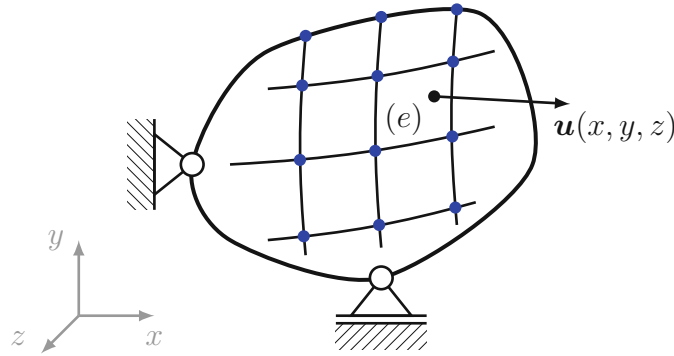


Figure 2.3: The system is discretized using finite elements

At this point, a special Ritz-ansatz is made for the displacement  $\mathbf{u}(x, y, z)$  within a finite element  $(e)$  [18, 17]:

$$\mathbf{u}(x, y, z) = \mathbf{N}^{(e)}(x, y, z) \mathbf{u}^{(e)}. \quad (2.41)$$

The displacement of a point  $P$  with the global coordinates  $(x, y, z)$  symbolized with  $\mathbf{u}(x, y, z)$  is approximated by using the nodal displacements  $\mathbf{u}^{(e)} = [u_{x_1}, u_{y_1}, u_{z_1}, u_{x_2}, \dots]$  of a finite element around this position and an interpolation matrix  $\mathbf{N}^{(e)}$  which yields a continuous field within the elements. The interpolating functions (also called shape functions) are components of the interpolation matrix  $\mathbf{N}^{(e)}$  and are in contrast to the general Ritz-method only valid within an element. Thus the shape functions are called local. The

shape functions are constructed so that the displacement  $\mathbf{u}(x, y, z)$  is always continuous between the elements ( $\mathcal{C}^0$  continuity must be ensured, see Section 2.2.3). Structural theories (beams, plates, shells) may require higher degree of continuity, namely  $\mathcal{C}^1$ -continuity, see Section 2.2.3.

What is the goal of this special Ritz-ansatz? It is implemented in the global equilibrium condition (2.40) and a solution for the nodal displacement  $\mathbf{u}^{(e)}$  of all elements is sought for, such that the equation is fulfilled in an approximate sense [18]. From that moment one has to keep in mind that this is only an approximation and no longer equal to the strong formulation. If the weak formulation (2.40) is used for a (cut out) finite element ( $e$ ) one gets in operator notation [18]

$$\int_{V^{(e)}} \boldsymbol{\sigma}_3^T \delta \boldsymbol{\varepsilon}_3 dV^{(e)} = (\mathbf{F}^{(e)})^T \delta \mathbf{u}^{(e)}, \quad (2.42)$$

with  $\boldsymbol{\sigma}_3 = [\sigma_{11}, \sigma_{22}, \sigma_{33}, \sigma_{23}, \sigma_{13}, \sigma_{12}]$  as the vector of stress components (Voigt-notation), the vector of strain components  $\boldsymbol{\varepsilon}_3 = [\varepsilon_{11}, \varepsilon_{22}, \varepsilon_{33}, 2\varepsilon_{23}, 2\varepsilon_{13}, 2\varepsilon_{12}]$  and the nodal force vector  $\mathbf{F}^{(e)} = \mathbf{F}_{\text{external}}^{(e)} + \mathbf{F}_{\text{internal}}^{(e)}$ . Distributed loads like  $\mathbf{k}_v$  and  $\mathbf{t}$  are converted into consistent nodal forces  $\mathbf{F}_{\text{external}}^{(e)}$  [17]. The nodal force vector  $\mathbf{F}^{(e)}$  includes in addition to the external forces also the internal forces (unknown) which became external forces on the considered cut out element ( $e$ ) [18].

In the next step of the derivation of the discrete linear FEM equation some expressions are used:

$$\begin{aligned} \boldsymbol{\varepsilon}_3 = (\nabla_3 \mathbf{u}_3)^S &= \frac{1}{2} [(\nabla_3 \mathbf{u}_3)^T + (\nabla_3 \mathbf{u}_3)] \rightarrow \boldsymbol{\varepsilon}_3 = \mathbf{d}\mathbf{u}_3 = \mathbf{dN}^{(e)} \mathbf{u}^{(e)} = \mathbf{D}^{(e)} \mathbf{u}^{(e)}, \\ \delta \boldsymbol{\varepsilon}_3 &= \mathbf{D}^{(e)} \delta \mathbf{u}^{(e)}, \end{aligned} \quad (2.43)$$

where  $\mathbf{D}^{(e)}$  denotes a differential operator matrix (operator notation) [18]. Furthermore Hooke's law (without temperature influence) is converted into operator notation too, where the elasticity tensor  ${}^4\mathbb{C}$  becomes the  $[6 \times 6]$  elasticity matrix  $\mathbf{E}$ :

$$\boldsymbol{\sigma}_3 = {}^4\mathbb{C} \cdot \cdot \boldsymbol{\varepsilon}_3 \rightarrow \boldsymbol{\sigma}_3 = \mathbf{E} \boldsymbol{\varepsilon}_3 = \mathbf{E} \mathbf{D}^{(e)} \mathbf{u}^{(e)}. \quad (2.44)$$

Inserting Equation (2.43) into (2.42) yields [18]

$$\int_{V^{(e)}} \boldsymbol{\sigma}_3^T \mathbf{D}^{(e)} dV^{(e)} = (\mathbf{F}^{(e)})^T. \quad (2.45)$$

Transposing both sides of Equation (2.45) and inserting (2.44) leads to an expression

for the element stiffness matrix  $\mathbf{K}^{(e)}$  [17]:

$$\boxed{\int_{V^{(e)}} \underbrace{(\mathbf{D}^{(e)})^T \mathbf{E} \mathbf{D}^{(e)}}_{\mathbf{K}^{(e)}} dV^{(e)} \mathbf{u}^{(e)} = \mathbf{F}^{(e)}}. \quad (2.46)$$

For dynamical analyses an element mass matrix is determined as [17]

$$\mathbf{M}^{(e)} = \int_{V^{(e)}} \rho^{(e)} \mathbf{N}^{(e)} (\mathbf{N}^{(e)})^T dV^{(e)}. \quad (2.47)$$

The nodal force vector  $\mathbf{F}^{(e)}$  still includes the internal forces  $\mathbf{F}_{\text{internal}}^{(e)}$  which are unknown, therefore one has to assemble all the finite elements ( $e$ ) to get rid of these [18]. At first, the element mass matrix  $\mathbf{M}^{(e)}$  and element stiffness matrix  $\mathbf{K}^{(e)}$  are evaluated using numerical integration (e.g. Gauss-Legendre Quadrature). For the assembly of all elements, in general a transformation from local to global coordinates as well as a mapping from local to global node numbering is necessary, reference is made to further literature [12]. Transformed quantities are signed with a tilde above. Now, the global matrices, the global nodal force vector and the global nodal displacements are calculated with

$$\mathbf{K} = \sum_{(e)} \tilde{\mathbf{K}}^{(e)}, \quad \mathbf{M} = \sum_{(e)} \tilde{\mathbf{M}}^{(e)}, \quad \mathbf{F} = \sum_{(e)} \tilde{\mathbf{F}}^{(e)}, \quad \mathbf{u} = \sum_{(e)} \tilde{\mathbf{u}}^{(e)}, \quad (2.48)$$

which yields the well known global system of equation for linear static problems:

$$\boxed{\mathbf{K} \mathbf{u} = \mathbf{F}}. \quad (2.49)$$

Subsequently the nodal displacements  $\mathbf{u}$  are obtained by solving the system of equations. Finally the strain and stress fields can be determined for the integration points within the element and extrapolated into the nodal points. The optimal points for the evaluation of derived variables from the displacement  $\mathbf{u}$  are the Gauss-Legendre integration points (Table 2.1) according to [10]. Strain and stress fields are in general not continuous over the element edges. This is a contradiction with the analytically solution, which would indicate an error in the approximate (FE) solution [10]. Therefore strains and stresses are often averaged on the element edges to get a continuous field [10].

### 2.2.2 Approach of this thesis for the plate problem

Using the advantages of computer algebra, we chose a faster way to obtain the two matrices  $\mathbf{K}$  and  $\mathbf{M}$ , which are necessary for the considered eigenvalue problem of the plate. We consider the quadratic forms of the kinetic energy  $T$  and strain energy  $U_b$  in linear systems to determine the global mass and stiffness matrix. At first  $T^{(e)}$  and  $U_b^{(e)}$ , the kinetic and strain energy of a finite element, are calculated. Afterwards, all finite elements are assembled with a mapping between the local and global numbering of nodes (and degrees of freedom) and the total quantities  $T$  and  $U_b$  are evaluated. The quadratic forms [20] with respect to the finite element method and the plate problem (Area  $A$ , plate thickness  $h$ , density  $\rho$ , transversal deflection  $w$ , rotary inertia of through-thickness elements is neglected in Kirchhoff's theory) read as

$$\begin{aligned} U_b^{(e)} &= \frac{1}{2} (\mathbf{q}^{(e)})^T \mathbf{K}^{(e)} \mathbf{q}^{(e)} = \frac{1}{2} \int_{A^{(e)}} D [\nu (\text{tr } \boldsymbol{\kappa}^{(e)})^2 + (1 - \nu) \boldsymbol{\kappa}^{(e)} \cdot \cdot \boldsymbol{\kappa}^{(e)}] dA^{(e)}, \\ T^{(e)} &= \frac{1}{2} (\dot{\mathbf{q}}^{(e)})^T \mathbf{M}^{(e)} \dot{\mathbf{q}}^{(e)} = \frac{1}{2} \int_{A^{(e)}} \rho h w^2 dA^{(e)}, \end{aligned} \quad (2.50)$$

where further  $\mathbf{K}$  and  $\mathbf{M}$  are obtained by

$$U_b = \sum_{(e)} U_b^{(e)}, \quad \mathbf{K} = \frac{\partial^2 U_b}{\partial q_i \partial q_j} \quad \text{and} \quad T = \sum_{(e)} T^{(e)}, \quad \mathbf{M} = \frac{\partial^2 T}{\partial \dot{q}_i \partial \dot{q}_j}. \quad (2.51)$$

In this formulation,  $\mathbf{q}$  denotes the generalized coordinate vector and  $\dot{\mathbf{q}}$  its time derivative (with superscript  $(e)$  only valid for a finite element). Integrals are calculated with Gauss-Legendre quadrature, which is discussed in the following section.

### 2.2.3 Local shape functions and numerical integration

In this section general aspects of local shape functions (two dimensional formulation) and the used procedure for the numerical integration are presented. The local shape functions together with the nodal displacements (special Ritz-ansatz (2.41)) describe the displacement field within a finite element  $(e)$ . Main advantages of this ansatz are the usage of a reference element with simple shape functions (transformation/mapping into unit square with normalized coordinates  $\xi, \eta$ ), further that the boundary conditions can be fulfilled easily and of course the numerical automation [18].

There are a few conditions to the shape functions [10]:

- Continuity - a field function must be continuous within the finite element ( $e$ ) and also across the element edges. Inside the element it is easy to ensure with a continuous function. The inter-element continuity is realised by setting the nodal displacements of neighbouring elements as equal and the usage of specially constructed shape functions  $\rightarrow \mathcal{C}^0$ -continuity. In the case of shear rigid beams, plates or shells it must be ensured that in addition to  $\mathcal{C}^0$  the first derivatives across the element boundaries are continuous too. This is called  $\mathcal{C}^1$ -continuity. Otherwise, the structure shows kinks which are physically not correct. The reason is that the curvature (second derivative) becomes infinite at kinks and therefore one would obtain squares of infinite terms in the strain energy [23].
- Shape functions  $N_i(\xi, \eta)$  must be linearly independent to obtain a unique solution.
- It must be possible to represent a gradient free field, which is in the mechanics of solids a rigid-body translation, for example. This is ensured with the so-called partition of unity:  $\sum_i N_i(\xi, \eta) = 1$ .
- The degree of a polynomial function has to be as high as necessary to get at least a constant value for the derivatives in the weak formulation.
- To ensure the displacement field  $\mathbf{u}$  at a node with coordinates  $\hat{\xi}_j$  is exactly the displacement of this node, the shape functions are constructed as given in (2.52). Therefore, the value of a shape function is exactly one at the respective node.

$$N_i(\hat{\xi}_j) = \begin{cases} 1 & \text{for } i = j \\ 0 & \text{for } i \neq j \end{cases} \quad (2.52)$$

There are a lot of possible types of shape functions, in most cases polynomial functions are used, see also [10]. The functions used in this thesis are given in Section 3.1.

The already mentioned transformation of the shape functions into a unit area is the next step towards increasing efficiency. Figure 2.4 shows the mapping from local and normalized (natural) coordinates  $\xi, \eta \in [-1, +1]$  into global coordinates with respect to the plate problem. At this point the shape functions were only used in context with displacements but they are of course also used to display the original geometry. If the same shape functions are used for the geometry and the displacement (each element is

transformed in the same way, hence:  $\mathbf{N}^{(e)} \rightarrow \mathbf{N}$ , plate problem is considered)

$$\mathbf{x} = \begin{bmatrix} x(\xi, \eta) \\ y(\xi, \eta) \\ 0 \end{bmatrix} = \mathbf{N}(\xi, \eta) \mathbf{x}^{(e)}, \quad \mathbf{u} = \begin{bmatrix} 0 \\ 0 \\ w(\xi, \eta) \end{bmatrix} = \mathbf{N}(\xi, \eta) \mathbf{u}^{(e)}, \quad (2.53)$$

then the elements are called isoparametric or one can say it is an isoparametric formulation [10]. When the order of the shape functions for the geometry is lower than for the displacement, it is called subparametric formulation [10]. In the case of higher order for the geometry it is a superparametric formulation [10].

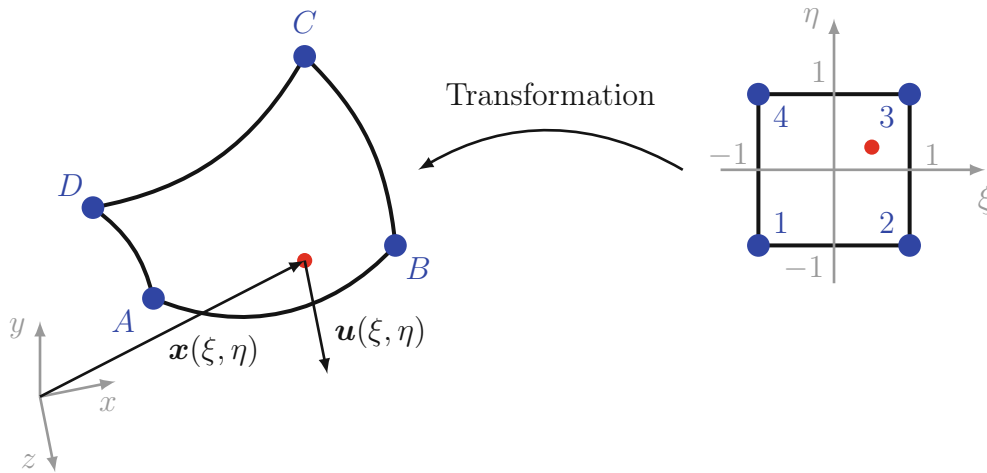


Figure 2.4: Mapping from local to global coordinates (plate problem)

As shown above, in the chosen approach to determine the global stiffness and mass matrix integrals of type

$$\int_{A^{(e)}} \mathbf{f}(x, y) dA^{(e)}, \quad (2.54)$$

have to be evaluated. Here  $\mathbf{f}(x, y)$  denotes an arbitrary function of global coordinates. Using the mapping into a unit square one can rewrite those integrals into [10]

$$\int_{A^{(e)}} \mathbf{f}(x, y) dA^{(e)} = \int_{-1}^{+1} \int_{-1}^{+1} \hat{\mathbf{f}}(\xi, \eta) \det \mathbf{J}(\xi, \eta) d\xi d\eta, \quad (2.55)$$

with  $\mathbf{J}(\xi, \eta)$  as the two-dimensional Jacobian:

$$\mathbf{J}(\xi, \eta) = \frac{\partial \mathbf{x}}{\partial \boldsymbol{\xi}} = \frac{\partial(x, y)}{\partial(\xi, \eta)} = \begin{bmatrix} \frac{\partial x}{\partial \xi} & \frac{\partial x}{\partial \eta} \\ \frac{\partial y}{\partial \xi} & \frac{\partial y}{\partial \eta} \end{bmatrix}. \quad (2.56)$$

Note that the presented variant of the Jacobian corresponds to a mathematical definition, contrary to many finite element literature sources (there it is defined as the transposed mathematical Jacobian) [10]. Next the occurring integrals are numerically evaluated using the Gauss-Legendre quadrature (often only named as Gauss-quadrature)[10]:

$$\int_{-1}^{+1} \int_{-1}^{+1} \hat{\mathbf{f}}(\xi, \eta) \det \mathbf{J} \, d\xi \, d\eta \approx \sum_{i=1}^{n_x} \sum_{j=1}^{n_y} \hat{\mathbf{f}}(\xi_i, \eta_j) \det \mathbf{J}(\xi_i, \eta_j) \omega_i \omega_j. \quad (2.57)$$

Here  $n$  is used for the number of integration points (integration order),  $(\xi_i, \eta_j)$  is the position of the integration points and  $\omega_{i,j}$  are the quadrature weights. Table 2.1 shows the position of the integration points, the maximum degree of a polynomial  $p_{max}$  which can be integrated analytically exact and the corresponding weights for  $\xi \in [-1, +1]$ .

Table 2.1: Gauss-Legendre parameters [10]

$n$	$p_{max}$	$\xi_i$	$\omega_i$
1	1	0	2
2	3	$\pm \frac{1}{\sqrt{3}}$	1
3	5	0 $\pm \sqrt{\frac{3}{5}}$	$\frac{8}{9}$ $\frac{5}{9}$
4	7	$\pm \frac{\sqrt{525-70\sqrt{30}}}{35}$ $\pm \frac{\sqrt{525+70\sqrt{30}}}{35}$	$\frac{1}{2} + \frac{\sqrt{30}}{36}$ $\frac{1}{2} - \frac{\sqrt{30}}{36}$

## 2.3 Energy approach to estimate changes in the natural frequencies

The standard modal analysis starts with the consideration of the unforced motion equation of a multiple degree of freedom (multiple DOF,  $\mathbf{q}$  as generalized coordinates) system:

$$\mathbf{M}\ddot{\mathbf{q}} + \mathbf{K}\mathbf{q} = \mathbf{0}. \quad (2.58)$$

With the determined mass and stiffness matrix the eigenvalue problem can be studied:

$$(\mathbf{K} - \omega^2\mathbf{M})\boldsymbol{\psi} = \mathbf{0}, \quad \det(\mathbf{K} - \omega^2\mathbf{M}) = 0. \quad (2.59)$$

Here  $\omega$  denotes the natural frequency (math: eigenvalue) and  $\boldsymbol{\psi}$  the corresponding mode shape (eigenmode, math: eigenvector). The characteristic equation  $\det(\mathbf{K} - \omega^2\mathbf{M}) = 0$  yields the natural frequencies. To each natural frequency there exists one (unique, except amplitude) mode shape vector  $\boldsymbol{\psi}$  (considering mechanical system which yields symmetric positive definite  $n \times n$ -matrices). Natural frequency and corresponding mode shape defines the so-called modal motion, which is a harmonic process [5]:

$$\mathbf{q} = \boldsymbol{\psi}e^{i\omega t}. \quad (2.60)$$

A general oscillation of a  $n$ -DOF system is then given as the sum of the modal motions with additional constants  $\alpha_k$  to fit the initial conditions [8]:

$$\mathbf{q} = \sum_{k=1}^n \alpha_k \boldsymbol{\psi}_k e^{i\omega_k t}. \quad (2.61)$$

An interesting question on this issue is: How do small changes in the elastic structure (additional masses or local damages) affect the natural frequencies? Is it necessary to execute another whole modal analysis for the perturbed system? To keep it short: No, a linear approximation exists. The derivation is now presented.

By solving (2.59) of the unperturbed system the natural frequencies  $\omega_0$  and the mode shapes  $\boldsymbol{\psi}_0$  are obtained. Assuming a small change in the mass and stiffness matrices (no influence on the kinematics, perturbed and original system have the same possible deformations,  $\mathbf{q}$  is used for both systems) we write with a small parameter  $\lambda$ :

$$\mathbf{K} = \mathbf{K}_0 + \lambda\mathbf{K}_1, \quad \mathbf{M} = \mathbf{M}_0 + \lambda\mathbf{M}_1. \quad (2.62)$$

Furthermore, the sought for natural frequency and mode shape can also be written with  $\lambda$  in terms of an asymptotic series

$$\omega = \omega_0 + \lambda\omega_1 + \mathcal{O}(\lambda^2), \quad \boldsymbol{\psi} = \boldsymbol{\psi}_0 + \lambda\boldsymbol{\psi}_1 + \mathcal{O}(\lambda^2). \quad (2.63)$$

Here,  $\omega_1$  and  $\boldsymbol{\psi}_1$  denote the first order correction. Consequently, the eigenvalue problem of the perturbed system becomes equal to

$$[\mathbf{K}_0 + \lambda\mathbf{K}_1 - (\omega_0 + \lambda\omega_1)^2(\mathbf{M}_0 + \lambda\mathbf{M}_1)](\boldsymbol{\psi}_0 + \lambda\boldsymbol{\psi}_1) = \mathbf{0}. \quad (2.64)$$

The equation is obviously fulfilled for the terms without  $\lambda$  because of the eigenvalue problem of the unperturbed problem

$$(\mathbf{K}_0 - \omega_0^2\mathbf{M}_0)\boldsymbol{\psi}_0 = \mathbf{0}. \quad (2.65)$$

All the terms with  $\lambda$  have to be equal to zero for the asymptotic series. Therefore one gets for the coefficients with  $\lambda$

$$(-\omega_0^2\mathbf{M}_1 - 2\omega_0\omega_1\mathbf{M}_0 + \mathbf{K}_1)\boldsymbol{\psi}_0 + (-\omega_0^2\mathbf{M}_0 + \mathbf{K}_0)\boldsymbol{\psi}_1 = \mathbf{0}. \quad (2.66)$$

Multiplying Equation (2.66) with  $\boldsymbol{\psi}_0^T$  from the left side and applying (2.65) yields

$$\boldsymbol{\psi}_0^T(-\omega_0^2\mathbf{M}_1 - 2\omega_0\omega_1\mathbf{M}_0 + \mathbf{K}_1)\boldsymbol{\psi}_0 = 0. \quad (2.67)$$

There one can see that the linear frequency correction  $\omega_1$  decouples from the mode shape correction  $\boldsymbol{\psi}_1$ . From that the searched frequency correction  $\omega_1$  is expressed as

$$\omega_1 = \frac{\boldsymbol{\psi}_0^T\mathbf{K}_1\boldsymbol{\psi}_0}{2\omega_0\boldsymbol{\psi}_0^T\mathbf{M}_0\boldsymbol{\psi}_0} - \frac{\omega_0\boldsymbol{\psi}_0^T\mathbf{M}_1\boldsymbol{\psi}_0}{2\boldsymbol{\psi}_0^T\mathbf{M}_0\boldsymbol{\psi}_0}. \quad (2.68)$$

Moreover the amplitude of the kinetic energy of the original system (value is equal to the amplitude of the strain energy) reads as

$$T_0 = \max_t \left( \frac{1}{2} \dot{\mathbf{q}}^T \mathbf{M}_0 \dot{\mathbf{q}} \right) = \frac{1}{2} \omega_0^2 \boldsymbol{\psi}_0^T \mathbf{M}_0 \boldsymbol{\psi}_0. \quad (2.69)$$

The kinetic energy of the added mass at a mode shape of the unperturbed system  $T_1$  and the additional strain energy of the perturbed system  $U_1$ , as a result of the stiffness

change are given by

$$T_1 = \frac{1}{2}\omega_0^2\boldsymbol{\psi}_0^T\mathbf{M}_1\boldsymbol{\psi}_0, \quad U_1 = \frac{1}{2}\boldsymbol{\psi}_0^T\mathbf{K}_1\boldsymbol{\psi}_0. \quad (2.70)$$

Finally, the first order frequency correction results in

$$\omega_1 = \frac{\omega_0}{2T_0}(U_1 - T_1), \quad \omega = \omega_0 + \omega_1. \quad (2.71)$$

To demonstrate the energy approach, a brief test is done using a simply supported Bernoulli-Euler beam with added concentrated mass  $\mu$  in the middle. The mass  $\mu$  determines the ratio of the added mass to the total mass of the beam. First the kinetic energies  $T_0$ ,  $T_1$  and the natural frequency  $\omega_0$  of the unperturbed beam have to be evaluated (first eigenmode is considered). Afterwards, a comparison of analytically exact solution and energy approach of the natural frequency of the perturbed system  $\omega$  can be plotted as shown in Figure 2.5. Here we see that the correspondence of exact solution and the prediction obtained by the energy approach is quite good up to  $\mu = 0.10$  (10%).

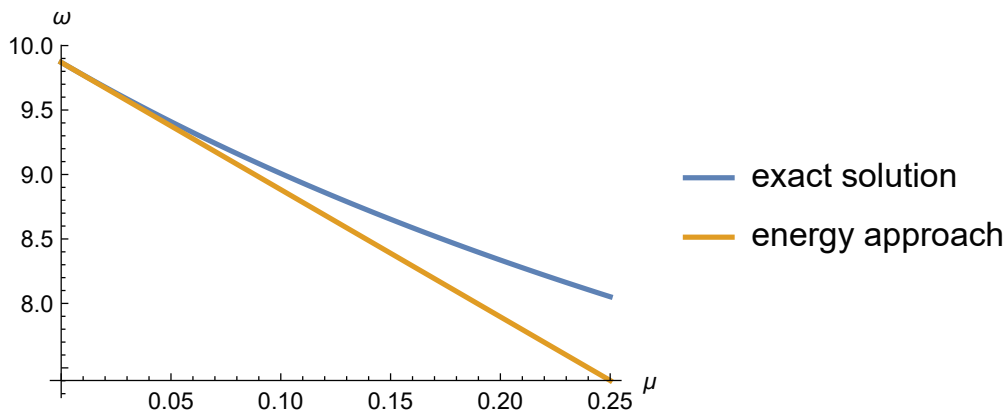


Figure 2.5: Beam with added mass: exact solution vs. energy approach, mode shape 1

# 3 Finite Element Model

## 3.1 Bogner-Fox-Schmit element formulation

As already mentioned in Section 2.2.3 the finite element approximation for a classical Kirchhoff plate must remain  $C^1$ -continuous under deformation. For this reason, quadrilateral  $C^1$ -continuous Bogner-Fox-Schmit (BFS) elements are used. These elements were introduced by Bogner, Fox and Schmit in the first conference on matrix methods in structural mechanics in 1965 [6, 7]. The BFS-elements (shown in Figure 3.1) own four corner-nodes with overall 16 degrees of freedom (four at each node). Consider a node  $i$  with the DOFs given by

$$w_i, \left(\frac{\partial w}{\partial \xi}\right)_i, \left(\frac{\partial w}{\partial \eta}\right)_i, \left(\frac{\partial^2 w}{\partial \xi \partial \eta}\right)_i, \quad (3.1)$$

with the nodal displacement (lateral displacement of the plate), the first derivatives in the two directions  $\xi$  and  $\eta$  and the second derivative.

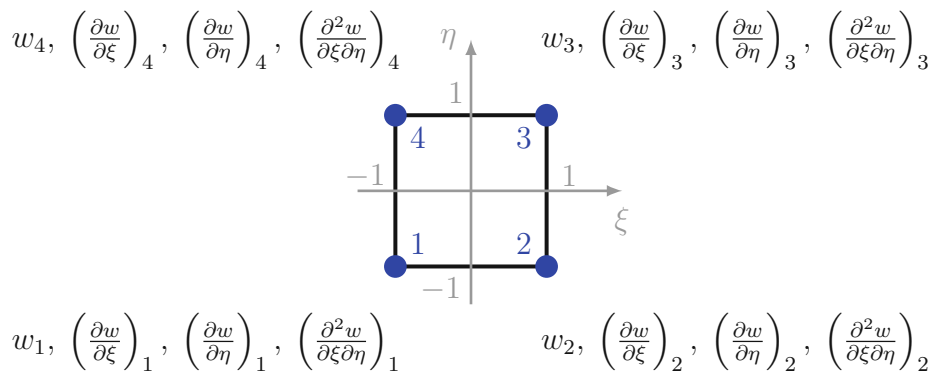


Figure 3.1: Square BFS-element with nodal DOFs and local coordinate system  $\xi - \eta$

At first glance, the second derivative as nodal DOF seems to be redundant but it can easily be shown that it is not. Therefore, we consider Figure 3.1 and examine the change of the first derivatives along the element edges. In general, the change of  $\partial w / \partial \xi$  along

the edge from node 1 to 4 (direction  $\eta$ ) is described with

$$\frac{\partial \frac{\partial w}{\partial \xi}}{\partial \eta} = \partial(\partial w / \partial \xi) \partial \eta, \quad (3.2)$$

which is only dependent on the nodal parameters 1 and 4. The same can be done for the edge from node 3 to 4 which leads to  $\partial(\partial w / \partial \eta) \partial \xi$ . At the common node 4, one can not automatically say that

$$\frac{\partial^2 w}{\partial \xi \partial \eta} \equiv \frac{\partial^2 w}{\partial \eta \partial \xi}, \quad (3.3)$$

for arbitrary nodal values 1 and 3 [23]. Hence it is impossible to determine polynomial shape functions which ensure full compatibility when only the displacement and its first derivatives are prescribed in the finite element nodes [23]. For this reason the mixed derivative  $\partial^2 w / \partial \xi \partial \eta$  is used as additional nodal parameter (DOF).

Furthermore BFS-elements are based on the use of Hermitian polynomials (known from shear rigid Bernoulli-Euler beam elements), thus they are one of the simplest approaches to obtain plate or shell elements. The one-dimensional cubic shape functions of the beam element (two nodes, see Figure 3.2) read as [6]

$$\begin{aligned} \psi_1 &= \frac{1}{4}(1 - \xi)^2(2 + \xi), & \psi_2 &= \frac{1}{4}(1 - \xi)^2(1 + \xi), \\ \psi_3 &= \frac{1}{4}(1 + \xi)^2(2 - \xi), & \psi_4 &= \frac{1}{4}(1 + \xi)^2(\xi - 1), \end{aligned} \quad (3.4)$$

with  $\xi$  as the local normalized coordinate. Here for example  $\psi_1$  corresponds to the displacement DOF of the node at  $\xi = -1$  and  $\psi_2$  to the rotational DOF at  $\xi = -1$  [6].

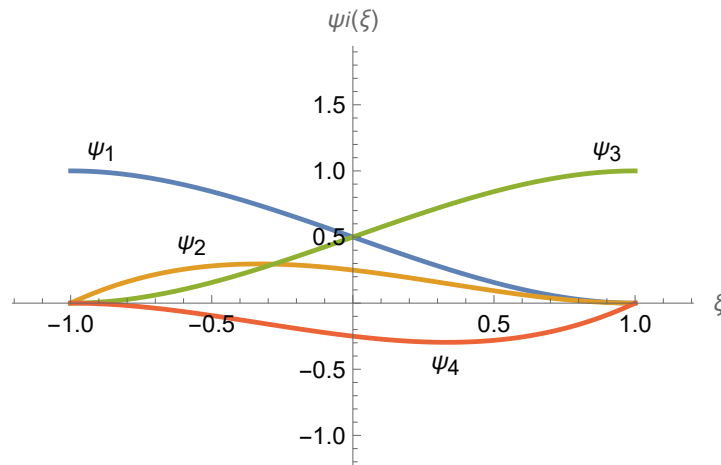


Figure 3.2: One-dimensional cubic Hermitian polynomials for shear rigid beam elements

The shape functions for the lateral deflection of a BFS-element at node  $i = 1$ , for example, are described with a second dimension  $\eta$  (local normalized coordinate) by the tensor products of the beam Hermitian polynomials (shown in Figure 3.3) [6]

$$\begin{aligned}
 S_{1,1} &= \psi_1(\xi)\psi_1(\eta) = \frac{1}{16}(1 - \xi)^2(2 + \xi)(1 - \eta)^2(2 + \eta), \\
 S_{1,2} &= \psi_2(\xi)\psi_1(\eta) = \frac{1}{16}(1 - \xi)^2(1 + \xi)(1 - \eta)^2(2 + \eta), \\
 S_{1,3} &= \psi_1(\xi)\psi_2(\eta) = \frac{1}{16}(1 - \xi)^2(2 + \xi)(1 - \eta)^2(1 + \eta), \\
 S_{1,4} &= \psi_2(\xi)\psi_2(\eta) = \frac{1}{16}(1 - \xi)^2(1 + \xi)(1 - \eta)^2(1 + \eta).
 \end{aligned} \tag{3.5}$$

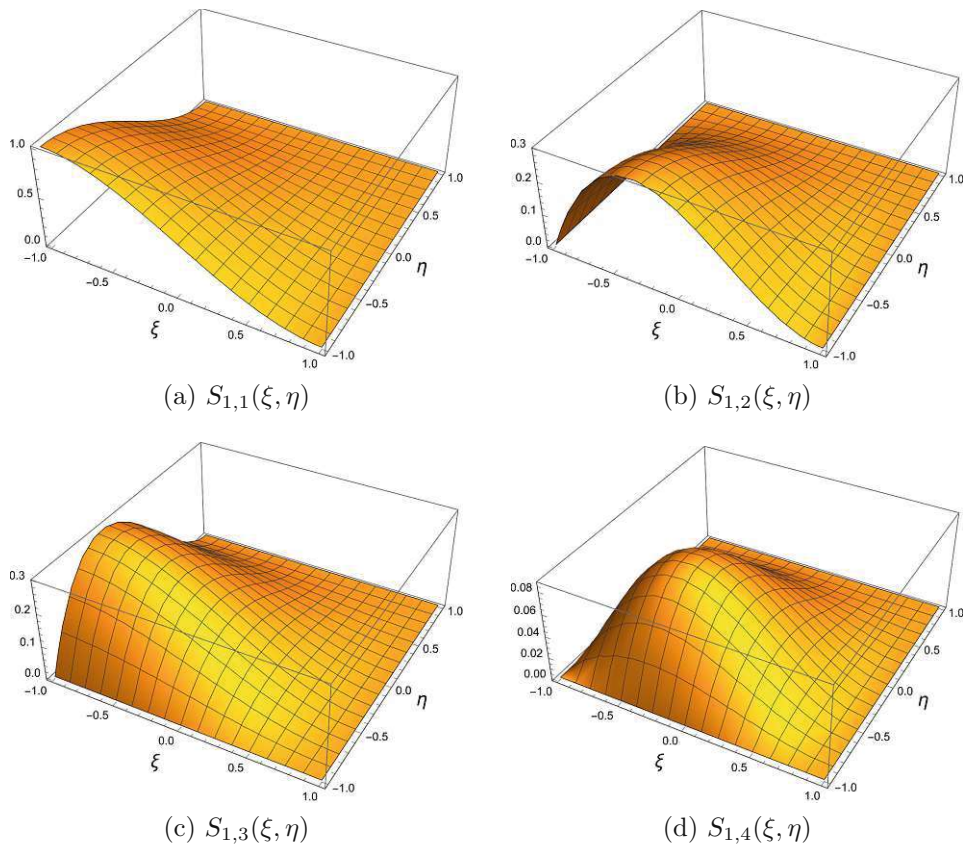


Figure 3.3: Bi-cubic shape functions of node 1 of a Bogner-Fox-Schmit element

Finally, the lateral deflection within a finite element is approximated with [6]

$$w(\xi, \eta) = \sum_{i=1}^4 \left[ w_i S_{i,1}(\xi, \eta) + \left( \frac{\partial w}{\partial \xi} \right)_i S_{i,2}(\xi, \eta) + \left( \frac{\partial w}{\partial \eta} \right)_i S_{i,3}(\xi, \eta) + \left( \frac{\partial^2 w}{\partial \xi \partial \eta} \right)_i S_{i,4}(\xi, \eta) \right]. \tag{3.6}$$

### 3.2 Rectangular mesh

In this thesis, rectangular and skewed meshes were implemented in Wolfram Mathematica for the examination of natural frequencies of a plate with additional mass or a crack. We begin with the implementation of the simple regular mesh, where the considered clamped square plate is discretized with square elements. As discussed above, the Bognner-Fox-Schmit finite elements were used. To increase the numerical efficiency we made also use of the mapping into a unit area with local coordinates, see also Section 2.2.3. The rectangular mesh with, for example,  $4 \times 4$  elements (element side length  $h = 0.25$  m) is depicted in Figure 3.4 (only the grid lines are shown). The parameters of the considered plate are: square plate with side length  $a = 1$  m, steel (density  $\rho = 7800$  kg/m<sup>3</sup>, Young's modulus  $E = 2.1 \cdot 10^{11}$  N/m<sup>2</sup>, Poisson's ratio  $\nu = 0.3$ ), thickness  $t = 10^{-3}$  m.

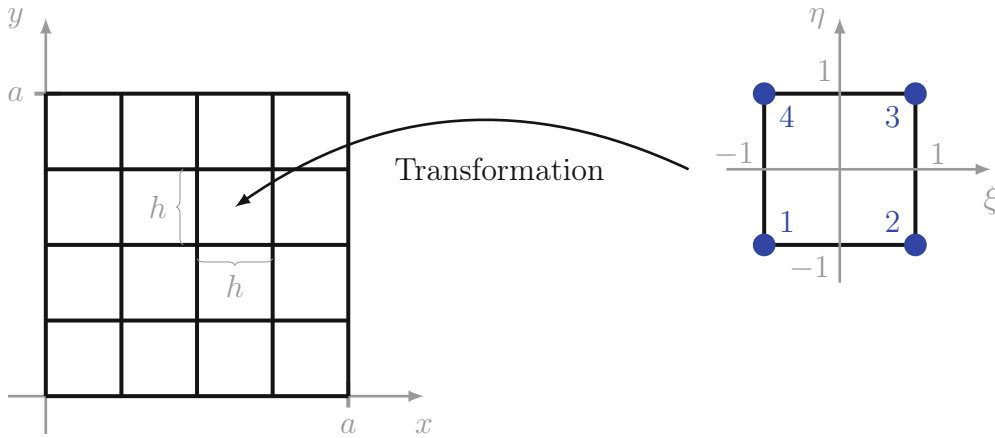


Figure 3.4: Rectangular mesh and mapping

With the approximation of  $w(\xi, \eta)$  (3.6) one can evaluate the kinetic energy  $T^{(e)}$  and strain energy  $U_b^{(e)}$  (2.50) for one finite element ( $e$ ). The necessary expression of the linearised curvature tensor for an element  $\kappa^{(e)}$  is determined as

$$\kappa^{(e)}(\xi, \eta) = \frac{4}{h^2} \nabla_{\xi\eta} \nabla_{\xi\eta} w(\xi, \eta). \quad (3.7)$$

Here the following relations are used

$$\begin{aligned} dx &= \frac{h}{2} d\xi, & dA &= dx dy = \frac{h^2}{4} d\xi d\eta, \\ dy &= \frac{h}{2} d\eta, & \nabla_{\xi\eta} &= \left[ \frac{\partial}{\partial \xi} \quad \frac{\partial}{\partial \eta} \right]^T. \end{aligned} \quad (3.8)$$

Subsequently, the expressions for  $U_b^{(e)}$  and  $T^{(e)}$  read as

$$U_b^{(e)} = \int_{A^{(e)}} u_b \, dA^{(e)} = \frac{1}{2} \int_{-1}^{+1} \int_{-1}^{+1} \frac{h^2}{4} D [\nu (\text{tr } \boldsymbol{\kappa}^{(e)})^2 + (1 - \nu) \boldsymbol{\kappa}^{(e)} \cdot \boldsymbol{\kappa}^{(e)}] \, d\xi \, d\eta, \quad (3.9)$$

$$T^{(e)} = \frac{1}{2} \int_{A^{(e)}} \rho t \dot{w}^2 \, dA^{(e)} = \frac{1}{2} \int_{-1}^{+1} \int_{-1}^{+1} \frac{h^2}{4} \rho t \dot{w}^2 \, d\xi \, d\eta.$$

The integrals are calculated with Gauss-Legendre quadrature using  $4 \times 4$  integrations points. After assembling the whole finite element model and taking into account the transformation from local DOFs into global DOFs (renumber the nodal DOFs), we write with a global vector of nodal DOF  $\mathbf{q} = \{q_i\}$  (see Section 2.2.2)

$$U_b = \sum_{(e)} U_b^{(e)}, \quad \mathbf{K} = \frac{\partial^2 U_b}{\partial q_i \partial q_j} \quad \text{and} \quad T = \sum_{(e)} T^{(e)}, \quad \mathbf{M} = \frac{\partial^2 T}{\partial \dot{q}_i \partial \dot{q}_j}. \quad (3.10)$$

Finally, the considered eigenvalue problem (2.59) yields the natural frequencies and mode shapes (first four given in Figure 3.5) for the unperturbed clamped square plate.

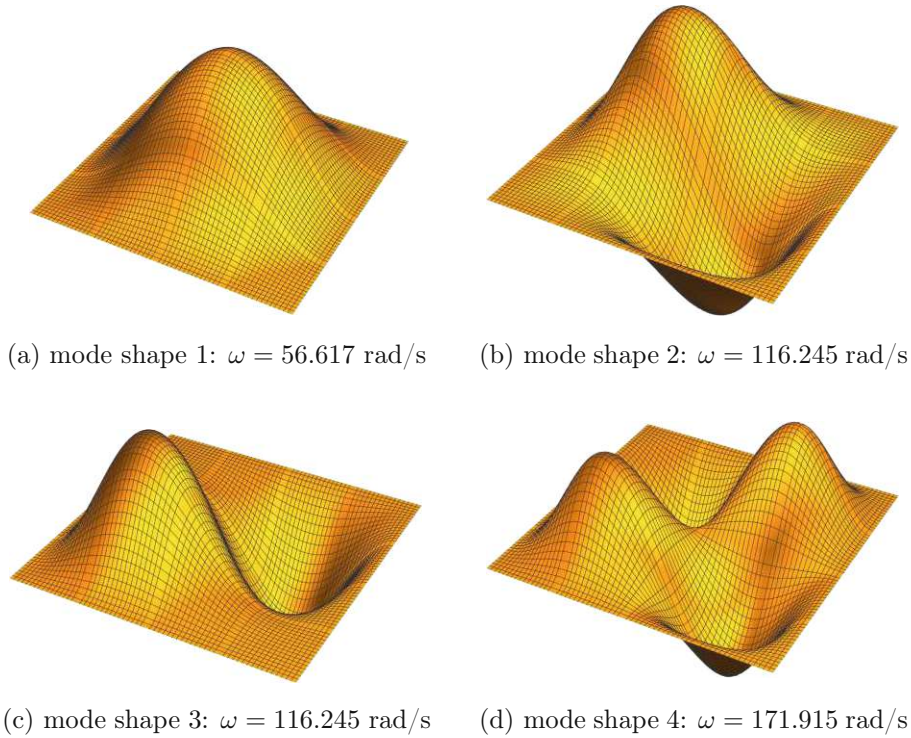


Figure 3.5: First four mode shapes with rectangular  $4 \times 4$  mesh

### 3.3 Skewed mesh

#### 3.3.1 The problem with the $\mathcal{C}^1$ -continuity

It gets more challenging to consistently treat the model with a skewed mesh with distorted elements. The skewed mesh will be used in further chapters when a reference solution for the case of cracks or added masses, which are not parallel to a plate edge, is searched. In this thesis, the skewed cracks or additional masses attached along a line are considered with an angle  $\alpha$  in the middle of the plate. How do the finite elements have to be changed to get a  $\mathcal{C}^1$ -continuous mesh? At first sight, it could be done with a well known bilinear transformation - as shown below it is unfortunately not sufficient. The sought for mapping for the unit element with local coordinates  $\xi, \eta$  into the global system  $x, y$  is sketched in Figure 3.6.

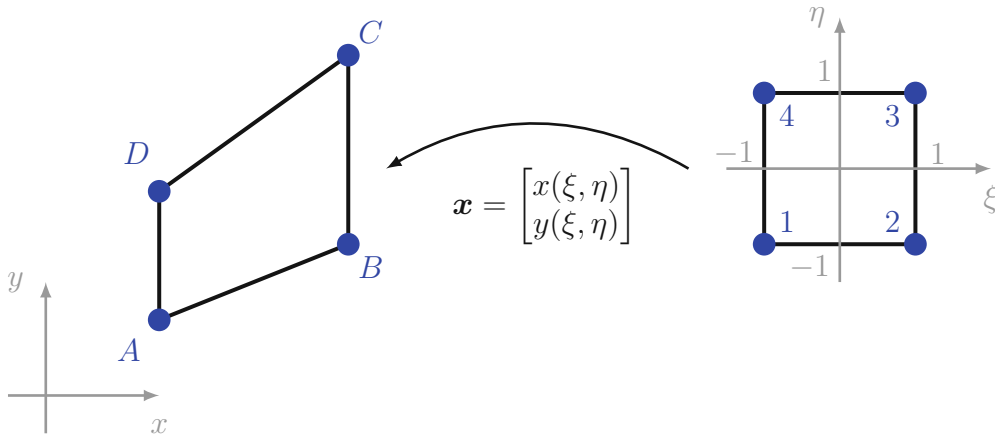


Figure 3.6: Mapping from local to global coordinates (skewed element)

An expression for the mapping  $\mathbf{x}$  (skew but straight element edges) is given by [10]

$$\mathbf{x} = \begin{bmatrix} x(\xi, \eta) \\ y(\xi, \eta) \end{bmatrix} = \mathbf{N}(\xi, \eta) \mathbf{x}^{(e)} = \begin{bmatrix} N_1 & 0 & N_2 & 0 & N_3 & 0 & N_4 & 0 \\ 0 & N_1 & 0 & N_2 & 0 & N_3 & 0 & N_4 \end{bmatrix} \begin{bmatrix} x_A \\ y_A \\ \vdots \\ x_D \\ y_D \end{bmatrix}, \quad (3.11)$$

where bilinear shape functions  $N_i$  are used to depict the geometry

$$\begin{aligned} N_1 &= 1/4(1 - \eta)(1 - \xi), & N_2 &= 1/4(1 - \eta)(1 + \xi), \\ N_3 &= 1/4(1 + \eta)(1 + \xi), & N_4 &= 1/4(1 + \eta)(1 - \xi). \end{aligned} \quad (3.12)$$

Instantly, the question arises how the mesh of the plate can be determined. The problem will be discussed with a simple sketch. Consider the square plate with a  $4 \times 4$  mesh, shown in Figure 3.7. The red grid line is inclined at the angle  $\alpha$ . Along this red line the crack or added mass are to be implemented.

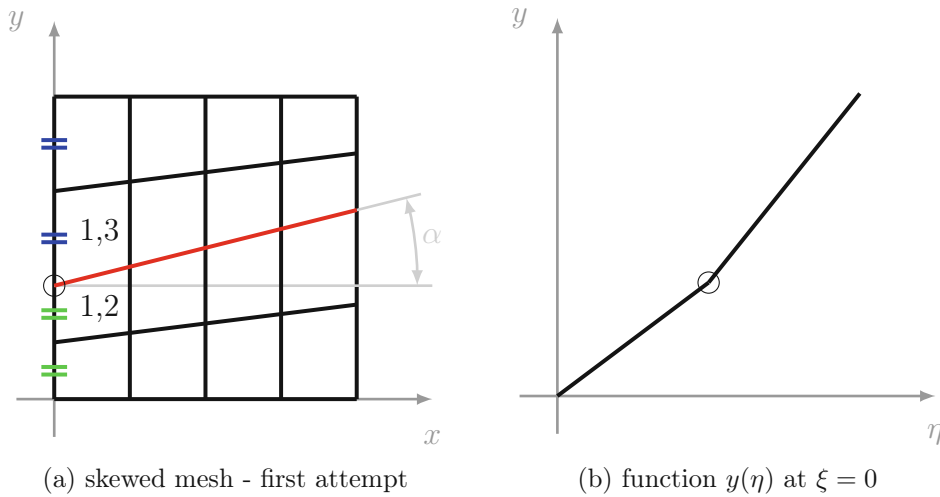


Figure 3.7: Sketch to point out the problem with the  $\mathcal{C}^1$ -continuity

In the easiest approach, one can set the element heights above and below as equal, as shown in Figure 3.7a with green and blue equal signs. The problem arises when two different element heights meet, for example element 1,2 and 1,3. Now we calculate the Jacobian  $\mathbf{J} = \partial \mathbf{x} / \partial \boldsymbol{\xi}$  for those two elements ( $\alpha = \pi/9$ ), evaluate them at a common node on the left edge (highlighted with a small circle), which yields

$$\mathbf{J}_{1,2}(\xi, \eta) \Big|_{\substack{\xi=-1 \\ \eta=+1}} = \begin{bmatrix} 0.125 & 0 \\ 0.0454963 & 0.0795037 \end{bmatrix} \neq \mathbf{J}_{1,3}(\xi, \eta) \Big|_{\substack{\xi=-1 \\ \eta=-1}} = \begin{bmatrix} 0.125 & 0 \\ 0.0454963 & 0.170496 \end{bmatrix}. \quad (3.13)$$

Comparing the elements  $\partial y / \partial \eta$  (matrix elements 2,2) of both Jacobians, it is now clear that the first derivatives are not equal with this mesh -  $\mathcal{C}^1$ -continuity is not ensured. In this case the function  $y(\eta)$  at  $\xi = 0$  shows a kink at the border of elements 1,2 and 1,3, sketched in Figure 3.7b. As a result, this easily constructed mesh is not going to yield physically exact solutions. Another approach to get a  $\mathcal{C}^1$ -continuous mesh must be found.

### 3.3.2 Double mapping – achieving $\mathcal{C}^1$ -continuity

In this section, we consider a double mapping intended to provide a remedy. Instead of the usual transformation from the unit area with local coordinates  $\xi, \eta$  directly into the physical domain  $x, y$ , another mapping is used inbetween. So, firstly, the new mapping will be a transformation from the unit area with coordinates which are now named as  $\xi_1, \eta_1 \in [-1, +1]$ , into a rectangular finite element within a mesh in coordinates  $\xi, \eta \in [0, 1]$  - analogous to Figure 3.4. Afterwards, the second transformation into the physical domain is done. We begin with the search for a  $\mathcal{C}^1$ -continuous mapping from the finite element mesh in into the physical domain. To obtain suitable functions  $x(\xi), y(\xi, \eta)$ , the mapping of two skewed elements (shown in Figure 3.8) is examined.

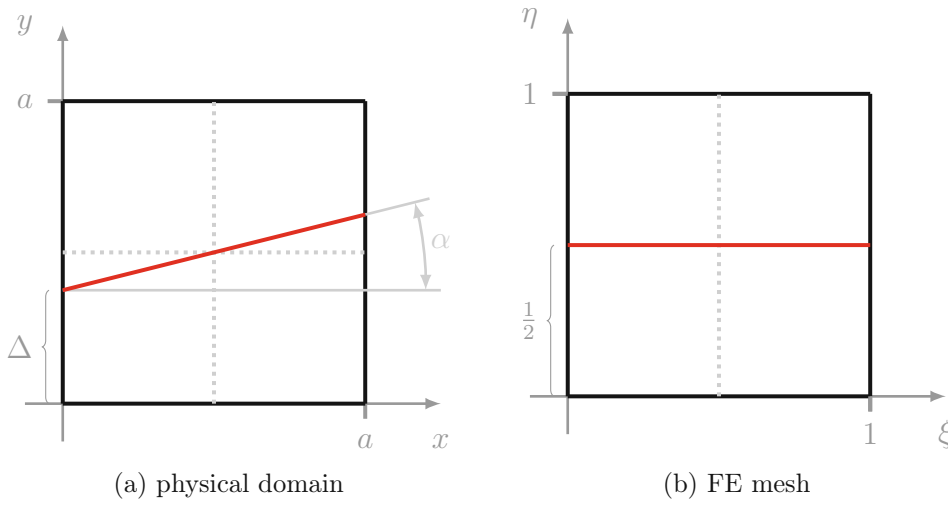


Figure 3.8: Sketch for the  $\mathcal{C}^1$ -continuous mapping  $(\xi, \eta) \rightarrow (x, y)$

Further the searched mapping is of the form

$$x(\xi) = a\xi, \quad y(\xi, \eta) = y_0(\eta)(1 - \xi) + y_1(\eta)\xi, \quad y_1 = a - y_0(1 - \eta), \quad (3.14)$$

where  $y_0$  and  $y_1$  are piecewise linear and cubic polynomials in  $\eta$ . With the given geometries in Figure 3.8 and an additional parameter  $\beta$ , which influences the gradient of the cubic polynomial, the solution for  $y_0(\eta)$  reads as

$$y_0(\eta) = \begin{cases} 2\eta\Delta & \eta < \frac{1}{2} \\ a[5 + 2\beta(-1 + \eta) - 4\eta](1 - 2\eta)^2 - \\ 2\Delta(-1 + \eta)[\beta(1 - 2\eta)^2 - 4(1 - 4\eta + 3\eta^2)] & \text{else.} \end{cases} \quad (3.15)$$

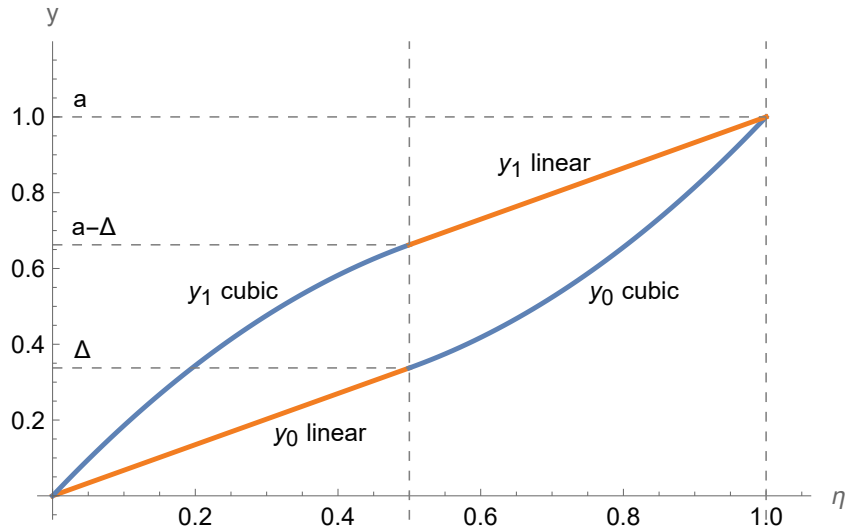


Figure 3.9:  $\mathcal{C}^1$ -continuous mapping  $\eta \rightarrow y$

Figure 3.9 shows the two functions  $y_0$  and  $y_1$ . They represent the  $y$ -transformation for the edges with  $\xi = 0$  and  $\xi = 1$ . The entire new mapping is depicted in Figure 3.10 for the case of  $8 \times 8$  finite elements, an angle  $\alpha = \pi/10$  and  $\beta = 1.5$ .

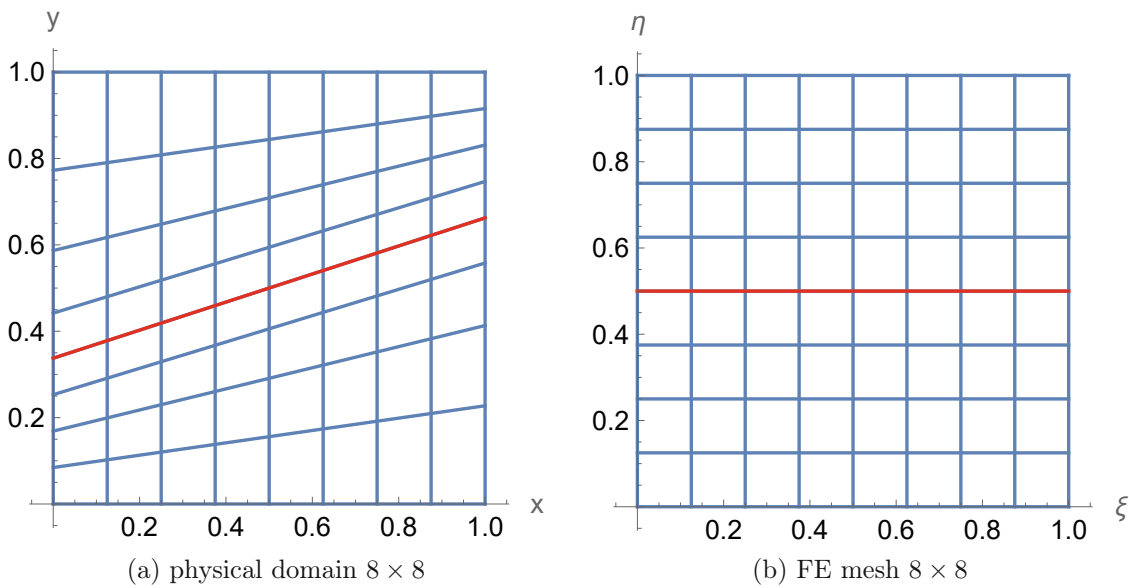


Figure 3.10:  $\mathcal{C}^1$ -continuous mapping from the FE mesh into the physical domain

On the left edge of the plate in the physical domain (Figure 3.10a) above the red grid line (cubic part of  $y_0$ ), we see the increase in element size along the  $y$ -axis, which is associated with  $\beta$ . Similar features to change the element size over a length are often called *bias* in commercial finite element programs. In this thesis,  $\beta = 1.5$  is chosen.

### 3.3.3 Eigenvalue problem

We aim at using the skewed mesh for the eigenfrequency analysis. At first the Jacobian  $\mathbf{J}(\xi, \eta)$  of the new mapping must be determined using the functions (3.14):

$$\mathbf{J}(\xi, \eta) = \frac{\partial(x, y)}{\partial(\xi, \eta)} = \begin{bmatrix} \frac{\partial x}{\partial \xi} & \frac{\partial x}{\partial \eta} \\ \frac{\partial y}{\partial \xi} & \frac{\partial y}{\partial \eta} \end{bmatrix}. \quad (3.16)$$

Here, one has to substitute the coordinates  $\xi, \eta$  expressed via the element number  $(i, j)$  and the local coordinates  $\xi_1, \eta_1$  to get the Jacobian as a function of  $\xi_1, \eta_1$ . The transformation from the unit area  $\xi_1, \eta_1 \in [-1, +1]$  into a rectangular finite element within the mesh in coordinates  $\xi, \eta \in [0, 1]$  is already known and can be adapted from Equations (3.7), (3.8). Thus, the linearised curvature tensor for an element  $\boldsymbol{\kappa}^{(e)}$  is determined as

$$\boldsymbol{\kappa}^{(e)}(\xi_1, \eta_1) = \frac{2}{h} \mathbf{J}^{-T}(\xi_1, \eta_1) \nabla_{\xi_1 \eta_1} \left[ \frac{2}{h} \mathbf{J}^{-T}(\xi_1, \eta_1) \nabla_{\xi_1 \eta_1} w(\xi_1, \eta_1) \right]. \quad (3.17)$$

With the determinant of the Jacobian  $\det \mathbf{J}(\xi_1, \eta_1)$  as a function of the local coordinates one can further write

$$\begin{aligned} U_b^{(e)} &= \frac{1}{2} \int_{-1}^{+1} \int_{-1}^{+1} \det \mathbf{J} \frac{h^2}{4} D [\nu (\text{tr } \boldsymbol{\kappa}^{(e)})^2 + (1 - \nu) \boldsymbol{\kappa}^{(e)} \cdot \cdot \boldsymbol{\kappa}^{(e)}] d\xi_1 d\eta_1, \\ T^{(e)} &= \frac{1}{2} \int_{-1}^{+1} \int_{-1}^{+1} \det \mathbf{J} \frac{h^2}{4} \rho t \dot{w}^2 d\xi_1 d\eta_1. \end{aligned} \quad (3.18)$$

For the integration a  $4 \times 4$  Gauss-Legendre quadrature is used. Consequently, we assemble the system and determine the eigenvalues with corresponding mode shapes - analogous to the rectangular mesh, see Equation (3.10). The mode shapes are similar, in the eigenvalues there are some differences though, especially for a smaller amount of finite elements. Therefore, in the following section a brief convergence study on those two meshes is done to show the differences.

## 3.4 Mesh convergence study

A quick convergence study is conducted with the rectangular and the skewed mesh before further calculations with added masses or cracks are done. The goal is to compare the values of the first four natural frequencies to check if the skewed mesh with the

double mapping converges to the same values as the rectangular mesh. The integration order was set to four. The parameters of the skewed mesh are unchanged ( $\alpha = \pi/10$ ,  $\beta = 1.5$ ). In Table 3.1 the numerical results of the convergence study are shown. The plate parameters are given in Section 3.2. Figures 3.11 and 3.12 display the convergence of the first natural frequency with rectangular and skewed mesh with a line plot. One can see that the rectangular mesh converges much faster than the skewed mesh. Furthermore, the calculation time was much shorter. Nevertheless, with  $8 \times 8$  or more finite elements the skewed mesh also yields accurate results. The relative difference between these two meshes in the first natural frequency with  $8 \times 8$  elements is 0.075%. Another interesting fact is that the rectangular mesh exhibits the repeated natural frequency (frequency two and three) even at  $2 \times 2$  finite elements. In contrast to the skewed mesh, the repeated frequency is not represented exactly here, even with  $16 \times 16$  elements.

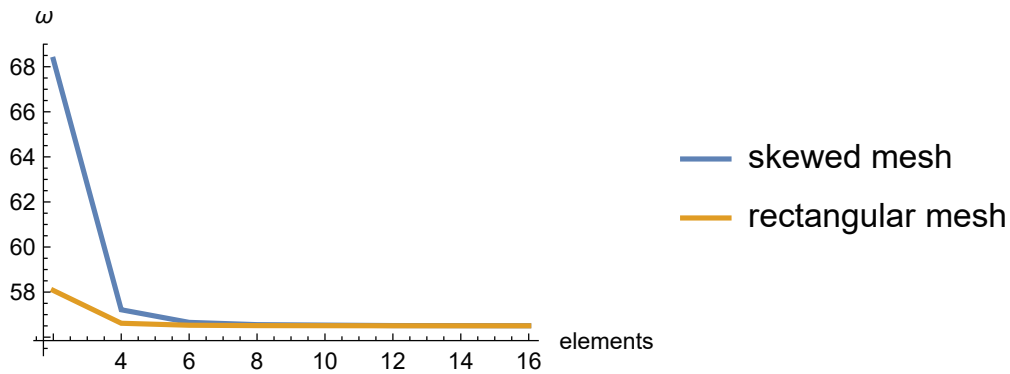


Figure 3.11: Convergence study

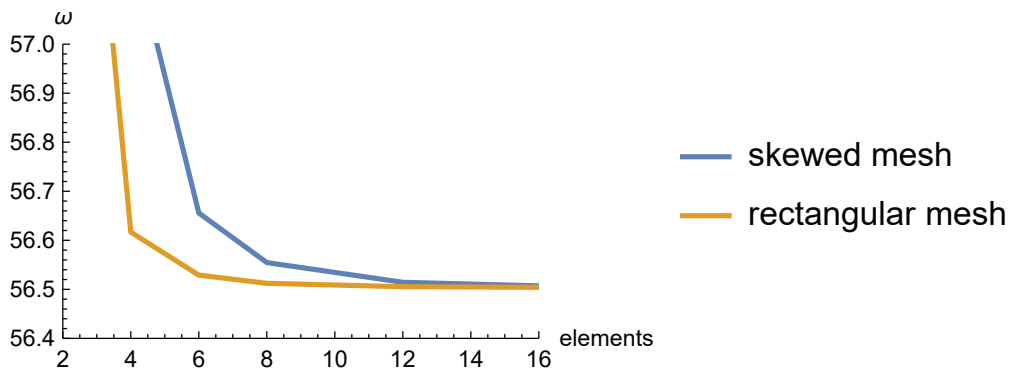


Figure 3.12: Convergence study, enlarged

Table 3.1: Convergence study: skewed - rectangular mesh

		Number of elements and mesh type					
		2 × 2		4 × 4		6 × 6	
		skewed	rectangular	skewed	rectangular	skewed	rectangular
<b>Eigenvalues</b>	<b>1.</b>	68.326	58.073	57.216	56.617	56.656	56.529
	<b>2.</b>	155.807	146.325	116.994	116.245	115.641	115.456
	<b>3.</b>	256.296	146.325	121.322	116.245	116.367	115.456
	<b>4.</b>	321.027	220.453	178.033	171.915	171.712	170.347

		Number of elements and mesh type					
		8 × 8		12 × 12		16 × 16	
		skewed	rectangular	skewed	rectangular	skewed	rectangular
<b>Eigenvalues</b>	<b>1.</b>	56.555	56.512	56.514	56.505	56.507	56.504
	<b>2.</b>	115.381	115.313	115.272	115.257	115.252	115.247
	<b>3.</b>	115.605	115.313	115.317	115.257	115.266	115.247
	<b>4.</b>	170.537	170.064	170.055	169.951	169.965	169.930

## 4 Plate with added line mass

In this chapter the energy approach, given in Section 2.3, is going to be tested for the square plate (clamped at all four edges) with added line masses. At first, the centric case is examined, where a line mass is applied in the middle of the plate parallel to an edge. Afterwards the line mass is inclined at an arbitrary angle  $\alpha < \pi/4$  to a plate edge and therefore no longer called centric. For each case the reference solution (line mass runs along element edges) is determined and compared to the energy approach. The plate parameters are: square plate with side length  $a = 1$  m, steel (density  $\rho = 7800$  kg/m<sup>3</sup>, Young's modulus  $E = 2.1 \cdot 10^{11}$  N/m<sup>2</sup>, Poisson's ratio  $\nu = 0.3$ ), thickness  $t = 10^{-3}$  m. The applied mass is described by a mass per unit length  $\mu$ .

### 4.1 Centric line mass

In the case of a centric line mass the reference solution and also the energy approach refer to the rectangular mesh ( $8 \times 8$  elements are used). The plate with applied line mass is shown in Figure 4.1 exemplary for the first two mode shapes.

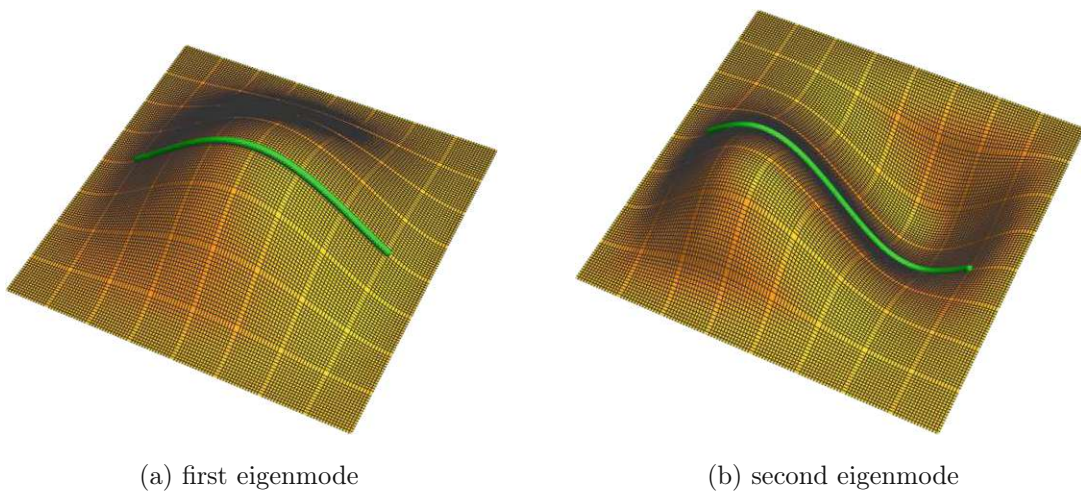


Figure 4.1: Centric line mass - plot on the first two eigenmodes

With the applied mass a new mass matrix  $\mathbf{M}$  is obtained, whereas the stiffness matrix  $\mathbf{K} = \mathbf{K}_0$  remains unchanged. Here we consider the added line mass as ideally flexible with zero bending stiffness ( $\Rightarrow U_1 = 0$  in the energy approach). The reference solution for the natural frequencies of the plate with the additional mass is determined by the eigenvalue problem. This calculation is repeated multiple times for different masses per unit length  $\mu$  and the resulting dependence is described by a curve.

For the energy approach, the kinetic energies of the unperturbed system  $T_0$  and of the applied mass  $T_1$  are required.  $T_0$  and  $T_1$  are already amplitudes by the definition, therefore we evaluate these kinetic energies by the use of the mode shapes. When the linear function of the energy approach is determined and the reference solution is known too, one can display them together. Figure 4.2 shows the comparison for the first mode shape of the plate, in Figure 4.3 the relative error of the first frequency is displayed.

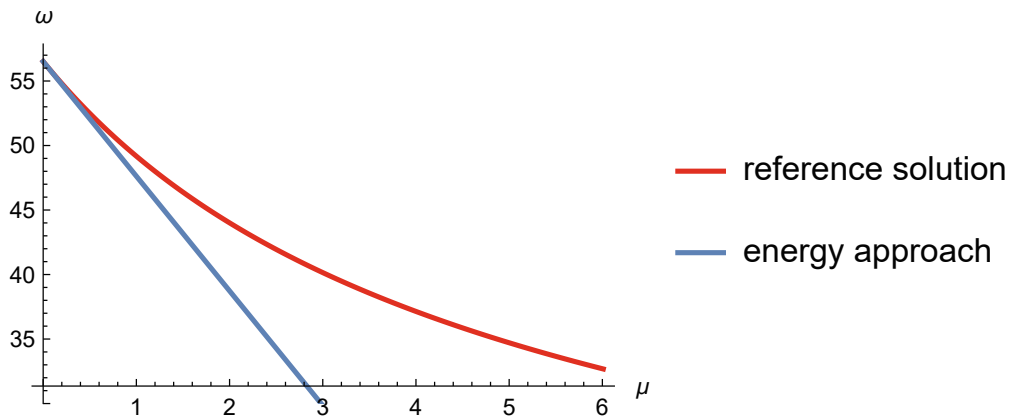


Figure 4.2: Centric line mass: reference solution vs. energy approach, mode shape 1

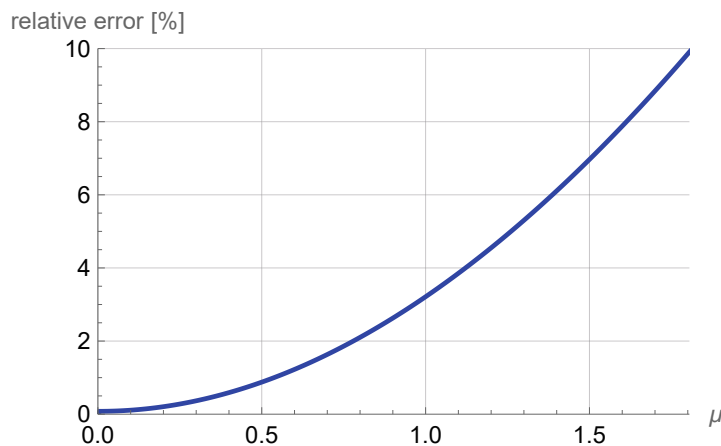


Figure 4.3: Relative error: centric line mass, mode shape 1

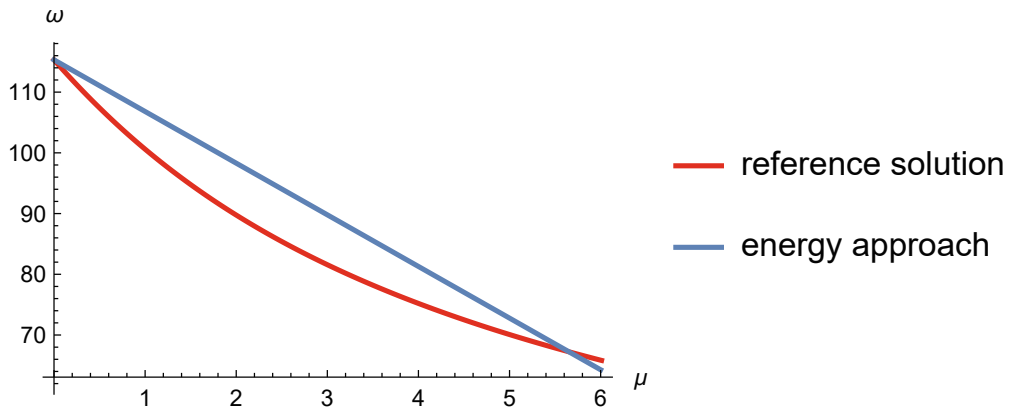


Figure 4.4: Centric line mass: reference solution vs. energy approach, mode shape 2

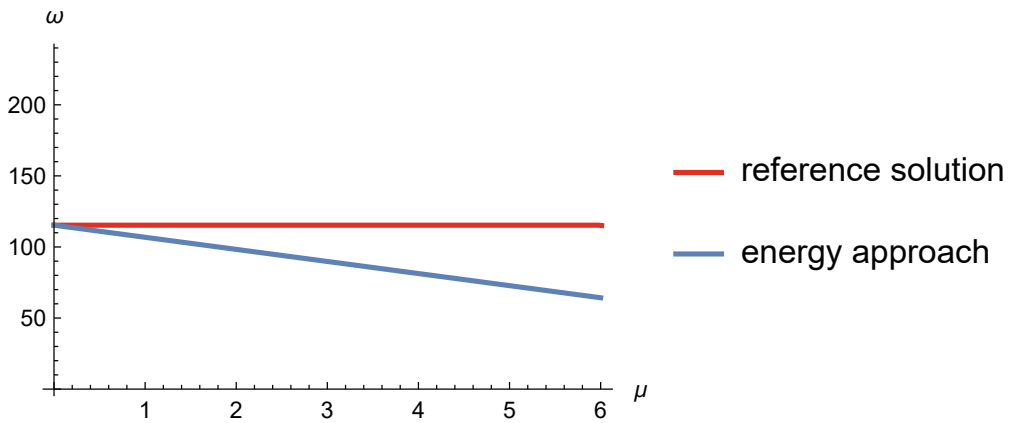


Figure 4.5: Centric line mass: reference solution vs. energy approach, mode shape 3

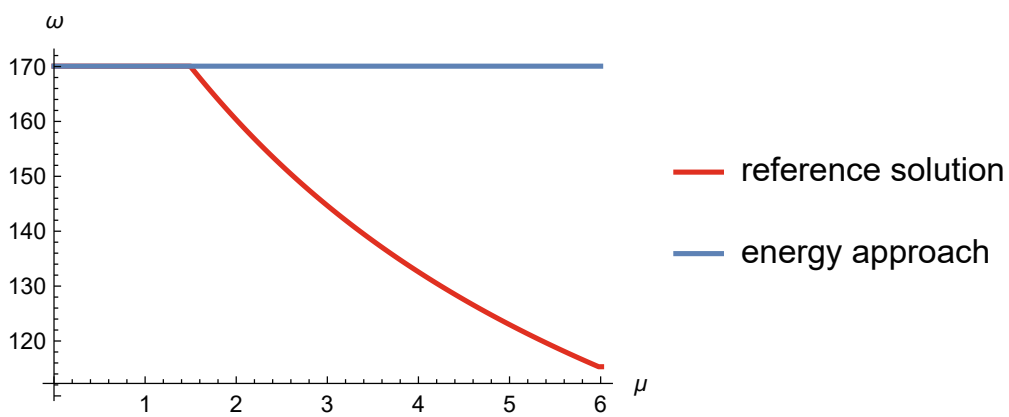


Figure 4.6: Centric line mass: reference solution vs. energy approach, mode shape 4

Table 4.1: Convergence study: initial slope - centric line mass, mode shape 1

	Number of elements and solution method			
	8 × 8		16 × 16	
	reference	energy approach	reference	energy approach
<b>Initial slope</b>	−8.8898	−8.8907	−8.8855	−8.8865

Furthermore, the mode shapes two to four are shown in Figures 4.4, 4.5 and 4.6. According to Figure 4.2, the energy approach describes the system for mode shape one at small values of  $\mu$  very well. As already expected, with increasing  $\mu$  the error between both solutions gets bigger. The relative error function in percent (with respect to the reference solution) for the first mode shape, as shown in Figure 4.3, gives a feeling how accurate the approach is. Here one can see for example at  $\mu = 1.260 \text{ kg/m}$  the relative error is 5%. Expressed in numerical values one deals with a plate mass of 7.8 kg and an applied line mass of 0.945 kg, which is approximately 12% of its own mass. By the examination of the initial slopes of both solutions in mode shape one the correspondence is also shown numerically. As initial slopes the first derivatives for  $\mu = 0$  are meant. For the reference solution the value of the slope was determined as good as possible using the difference quotient. The slope of the linear function of the energy approach is given by  $\omega_1$  in Equation (2.71). In Table 4.1 the values of the initial slopes are compared for two different meshes, the length of the applied mass is in both cases the same. With a  $16 \times 16$  mesh the correspondence is already very good. Hence there is good convergence. In Figures 4.4 and 4.5 it is clearly shown, that the energy approach for the second and third mode shapes does not reflect the systems behaviour, the slopes for  $\mu = 0$  are not the same. The fourth mode shape is also well approximated until the kink in the reference solution occurs.

So what is the problem? Further calculations showed that at repeated natural frequencies (two equal eigenvalues with different mode shapes) the energy approach in its presented simple form fails. Considering the first ten eigenvalues and mode shapes for the square plate, the second and third, also the seventh and eighth, as well as the ninth and tenth eigenvalue are the same. In all these cases the energy approach fails.

## 4.2 Skewed line mass

In the next step the plate is loaded with a line mass applied at an angle  $\alpha = \pi/6$  to the center. In this case, one cannot obtain a reference solution with the rectangular mesh. A skewed mesh is needed, where the added mass is aligned with the element edges. The solution for the energy approach is again evaluated with the regular mesh. For the energy approach the kinetic energy of the applied mass  $T_1$  was calculated by numerical integration using the trapezoidal rule. Both meshes contain  $8 \times 8$  elements. Figure 4.7 shows the applied mass on the rectangular mesh. A comparison of both solutions for the first four mode shapes is shown in Figures 4.8, 4.9, 4.10 and 4.11.

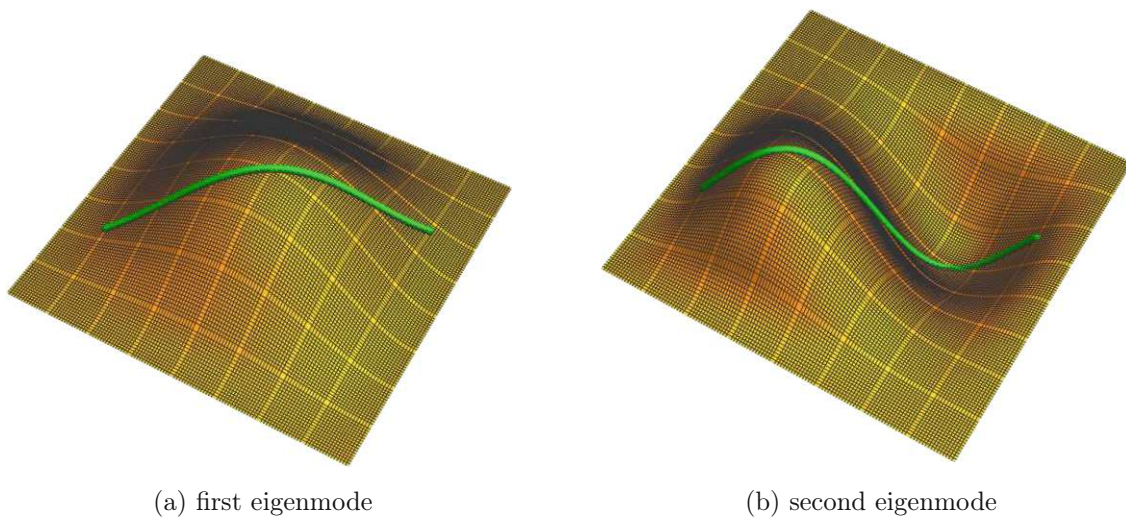


Figure 4.7: Skewed line mass - plot on the first two eigenmodes

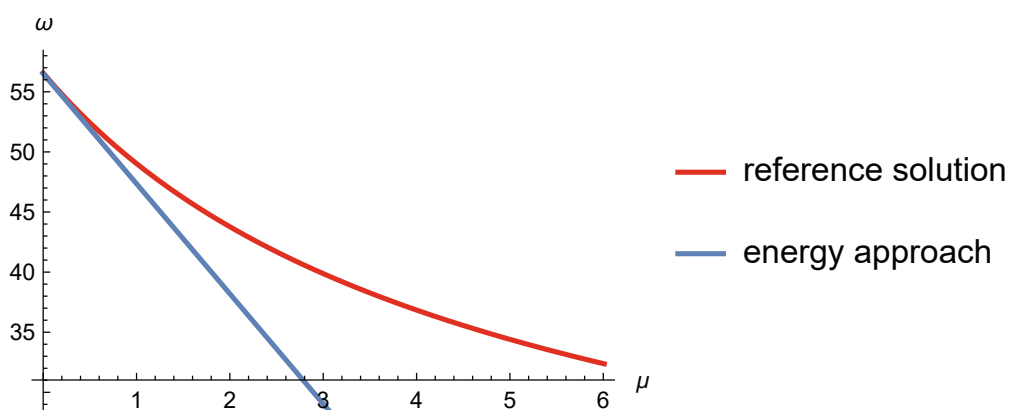


Figure 4.8: Skewed line mass: reference solution vs. energy approach, mode shape 1

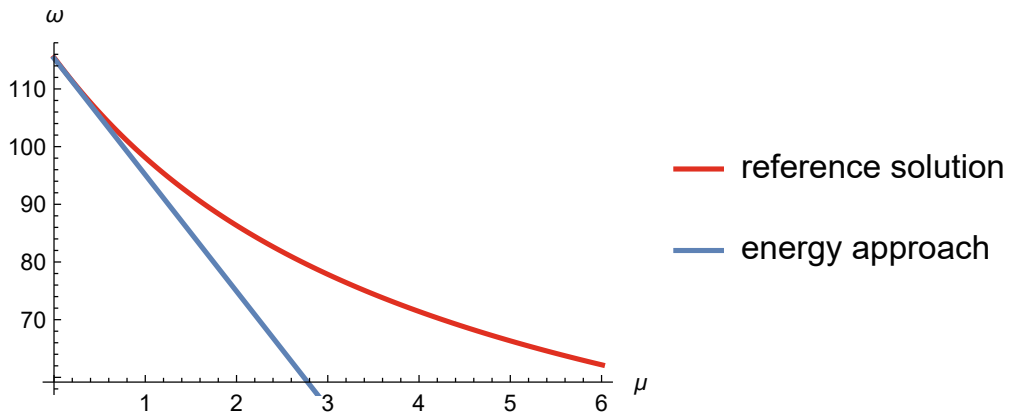


Figure 4.9: Skewed line mass: reference solution vs. energy approach, mode shape 2

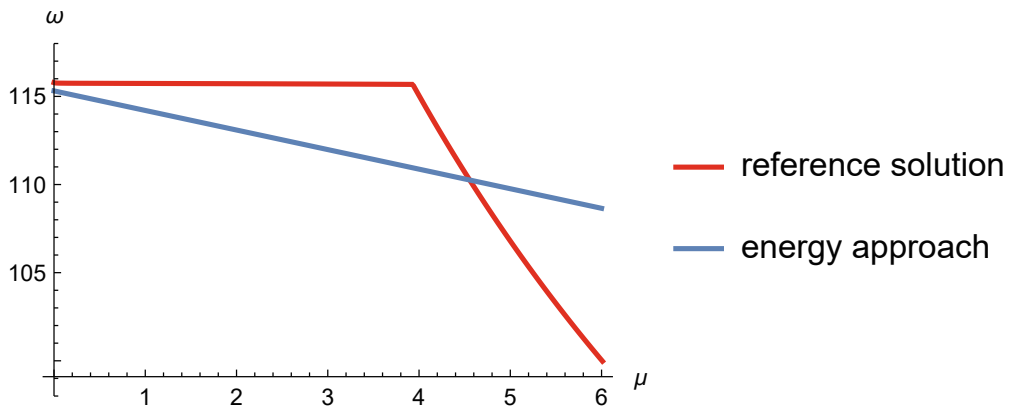


Figure 4.10: Skewed line mass: reference solution vs. energy approach, mode shape 3

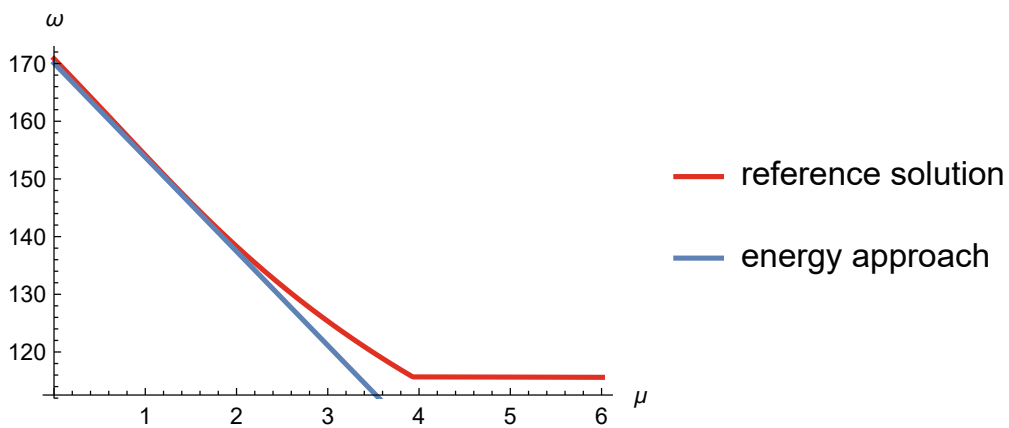


Figure 4.11: Skewed line mass: reference solution vs. energy approach, mode shape 4

Table 4.2: Convergence study: initial slope - skewed line mass, mode shape 1

	Number of elements and solution method			
	8 × 8		16 × 16	
	reference	energy approach	reference	energy approach
<b>Initial slope</b>	-9.1806	-9.1582	-9.1573	-9.1560

The first mode shape is approximated very well by the energy approach according to Figure 4.8. Similar to the centric line mass, the initial slopes are again numerically determined and compared to each other. Table 4.2 shows a comparison of the initial slopes of reference solution and energy approach for mode shape one in the case of a skewed line mass. An interesting fact is that the energy approach is more accurate at  $8 \times 8$  elements than the reference solution. This is a result of the slow convergence of the skewed mesh. At  $16 \times 16$  finite elements the values of the slopes differ only in the third decimal place. Overall one can say that for the first mode shape the convergence of the reference solution and energy approach is quite good. In contrast to the centric line mass, it seems that the second mode shape (Figure 4.9) is also well approximated with the energy approach. Further calculations showed that this behaviour occurs not every time. There is a dependence on the mesh size and length of the line mass which influences the result. Anyway, the third mode shape in Figure 4.10 proves that the energy approach also fails at repeated natural frequencies for skewed line masses. Again, like in the case of the centric line mass, the fourth mode shape (single eigenvalue) is approximated quite good.

To sum up, natural frequencies of a plate with added line mass can only be approximated by the energy approach for unique eigenvalues. At repeated eigenvalues the energy approach fails. Is this failure also obtained when a crack is considered instead of the applied line mass? The following chapter deals with this question.

# 5 Cracked plate

In an analogous way to the applied line mass, the energy approach is now tested for the clamped square plate with a crack along a line. We start with some basic ideas of the mechanical modelling, the implementation of the crack into the finite element model and the used expression for the energy approach. Following this, the centric case is considered, where the crack runs in the middle of the plate parallel to an edge. Afterwards, a skewed crack (inclined at an arbitrary angle  $\alpha < \pi/4$  to the plate edge) is examined. For each case the reference solution (element edges are aligned with the line of the crack) is compared to the energy approach. The plate parameters remain unchanged: square plate, side length  $a = 1$  m, steel (density  $\rho = 7800$  kg/m<sup>3</sup>, Young's modulus  $E = 2.1 \cdot 10^{11}$  N/m<sup>2</sup>, Poisson's ratio  $\nu = 0.3$ ), thickness  $t = 10^{-3}$  m.

## 5.1 Crack implementation and adapted energy approach

In this thesis a non-through-thickness crack is examined. In particular, a symmetric crack at the top and bottom surfaces of the plate is considered, which results in a local compliance. As a result, the displacement of the plate  $w(x, y)$  must be continuous ( $\mathcal{C}^0$ ) at the crack location, but may have slope discontinuities there, which is kinematically inadmissible in the ideal plate with no damage. Such cracks are conventionally modelled in mechanics by a hinge with a rotational spring (stiffness  $c_T$ , massless). The rotational spring acts against the slope difference at the shores of the crack. Of course, for high values of  $c_T$  the unperturbed solution must be approached.

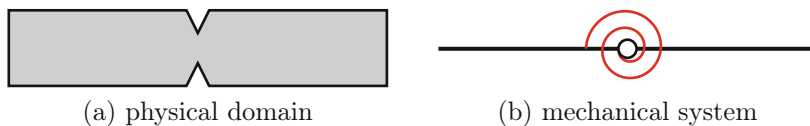


Figure 5.1: Mechanical modelling: non-through-thickness crack

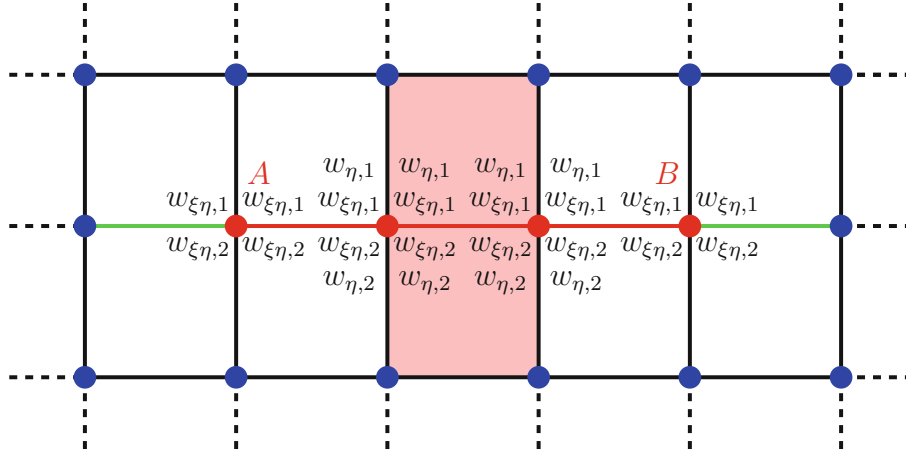


Figure 5.2: Crack implementation in the FE-model - split up degrees of freedom

The mechanical modelling is sketched in Figure 5.1, where the cross sections of the crack in the physical domain and in the mechanical system are compared. To implement the crack into the finite element model, we have to split up degrees of freedom at its location and introduce new ones to allow the plate to show up a kink (slope difference,  $C^1$ -continuity is no longer valid). In Figure 5.2 the splitting of the DOFs is sketched for the centric case. The crack (between nodes  $A$  and  $B$ ) is represented with the red element edges and nodes. There are two elements highlighted in light red, where the crack is fully developed along the common element edge. Transition elements are symbolized with a green element edge, where the crack arises/disappears. The separated degrees of freedom (written next to the corresponding nodes,  $\partial w / \partial \eta = w_{\eta}$ ,  $\partial^2 w / (\partial \xi \partial \eta) = w_{\xi\eta}$ ) are distinguished with index one and two for upper and lower shores at the crack. To keep the sketch simple, no global numbering of nodes is given. Furthermore, all the other unchanged DOFs are not mentioned. A new routine is necessary for the assembly of all finite elements, with special attention to the new DOFs. These DOFs are connected through the rotational spring along the crack. The total kinetic energy  $T$  and bending strain energy  $U_b$  of the plate are calculated straight forward, see Equations (2.50) and (2.51). For the total elastic energy  $U = U_b + U_s$  one has to consider the contribution of the rotational spring  $U_s$  as well. The expression for  $U_s$  differs for the centric and skewed cases and is discussed in the corresponding Sections 5.2.1 and 5.3.1. Using  $U$  and  $T$  one can calculate the global mass and stiffness matrix analogous to Equation (2.51).

Instantly, the question arises: how to correctly use the energy approach in the case of cracks? The expression for the frequency correction (2.71) needs to be adjusted now. This expression is used for an additional stiffness or mass. Here in the case of

a crack, an additional compliance is added to the system, hence we can no longer use Equation (2.71). This is because the vibration mode of the ideal plate results in no slope difference in the crack as it is  $\mathcal{C}^1$ -continuous. Instead of the additional strain energy  $U_1$ , the complementary energy of the rotational spring  $U^*$  is needed. The reason is simple,  $U_1$  due to the rotational spring can only be determined with the global vector of nodal DOFs of the cracked plate. Of course, this is not the goal when applying the energy approach. In [9] a mathematical justification using continuum mechanics considerations for a general valid energy approach formula is given. Referring to [9], an analogous variant of the energy approach (2.71) which is valid for additional compliance (cracks) is given by (note the additional negative sign):

$$\omega_1 = -\frac{\omega_0 U^*}{2T_0}, \quad \omega = \omega_0 + \omega_1. \quad (5.1)$$

Here all quantities are evaluated using the simple rectangular mesh. The calculation of the complementary energy  $U^*$  differs for the centric and skewed cases and is therefore given in the corresponding Sections 5.2.1 and 5.3.1.

## 5.2 Centric crack

### 5.2.1 Potential of the spring and complementary energy

Using the presented implementation of a non-through-thickness crack we start with the examination of the centric case. The potential energy of the rotational spring along the crack is described by an integral over the crack length  $L = \overline{AB}$

$$U_s = \frac{1}{2} c_T \int_L \left[ \frac{2}{h} \left( \frac{\partial w}{\partial \eta} \right)_1 - \frac{2}{h} \left( \frac{\partial w}{\partial \eta} \right)_2 \right]^2 ds. \quad (5.2)$$

Here  $(\partial w / \partial \eta)_1$  and  $(\partial w / \partial \eta)_2$  represent the slopes at the upper (index one) and lower (index two) shores of the crack. The crack length  $L = \overline{AB}$  is shown in Figure 5.2. With determined  $U_s$  we are able to calculate the global mass and stiffness matrix and further the eigenvalue problem of the cracked plate.

For the calculation of the complementary energy of the spring  $U^*$  one needs the tensor of moments  $\mathbf{m}$  of the unperturbed plate (2.21). The relevant component of  $\mathbf{m}$  is the bending moment  $M_{22} = M_{yy}$  which is to be determined along the location of the crack (unperturbed finite element model).  $M_{yy}$  can be calculated with the upper ( $\eta = -1$ ) or lower ( $\eta = +1$ ) finite elements at the crack. We distinguish them with  $M_{yy1}$  above

and  $M_{yy2}$  below the crack. Their values are different because the curvature is slightly discontinuous. Thus, to increase the accuracy, the arithmetic mean of  $M_{yy1}$  and  $M_{yy2}$  was evaluated and used for  $U^*$ . The complementary energy  $U^*$  of the rotational spring for the centric crack is given by

$$U^* = \frac{1}{2} \int_L \left( \frac{M_{yy1} + M_{yy2}}{2} \right)^2 \lambda \, ds, \quad (5.3)$$

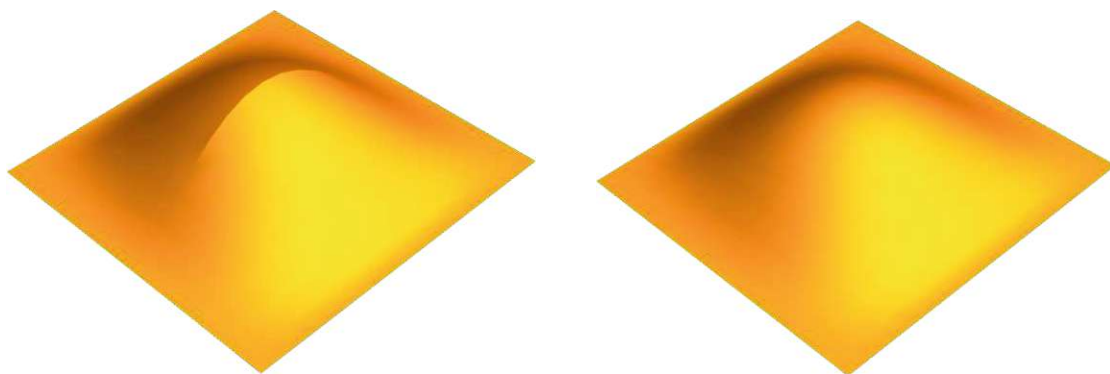
where  $\lambda = 1/c_T$  is the small compliance of the rotational spring. With the potential and complementary energy of the spring all quantities are known to obtain the reference solution and energy approach for the centric crack.

### 5.2.2 Testing the cracked finite element model

Before the natural frequencies are calculated, we do a brief plausibility check of the behaviour of the cracked finite element model. Therefore, the static deflection of the cracked plate due to gravity is determined for two different values of spring stiffness  $c_T$  (low and high value). We consider a crack in the middle of the plate with length  $L = 0.5a$ . The static solution is then obtained by using the potential of external forces  $W$  and with the following relations:

$$W^{(e)} = \int_{A^{(e)}} \rho t g w \, dA^{(e)}, \quad W = \sum_{(e)} W^{(e)}, \quad \mathbf{F} = -\frac{\partial W}{\partial \mathbf{q}}, \quad \mathbf{K} \mathbf{q}_{static} = \mathbf{F}. \quad (5.4)$$

Here  $g$  is the free fall acceleration and  $\mathbf{q}$  is the global vector of nodal degree of freedoms (the active ones). Both solutions are scaled by a factor of -50 and shown in Figure 5.3.



(a) low stiffness  $c_T = 10^2$  - a kink occurs

(b) high stiffness  $c_T = 10^8$  - smooth surface

Figure 5.3: Centric crack - comparison of static deflection, hidden rectangular mesh

With such a three-dimensional plot of the plate one can observe the kink, which is visible in the case of smaller spring stiffness, see Figure 5.3a. In contrast, with higher stiffness the function of the hinge is suppressed and an increasingly smoother surface occurs, which looks like the unperturbed system (Figure 5.3b). To check the correspondence of unperturbed plate and cracked plate with high spring stiffness ( $c_T = 10^8$ ,  $L = 0.5a$ ) numerically, the values of the static deflection in the middle of the plate are compared in Table 5.1. Here we clearly see that the correspondence is very good.

Table 5.1: Convergence study: max. static deflection,  $32 \times 32$  elements

Cracked plate:  $c_T = 10^8$ ,  $L = 0.5a$   $w_{\max} = -0.005034622516$  m

Unperturbed plate  $w_{\max} = -0.005034621270$  m

### 5.2.3 Comparison of reference solution and energy approach

Now the energy approach (5.1) is applied and the results are compared to the reference solution in the case of a centric crack. We consider a crack in the center of the square plate with a length  $L = 0.5a$ , like in Figure 5.3. For the analysis a rectangular mesh with  $32 \times 32$  elements was chosen. The reason for this fine mesh is the slower convergence of the cracked finite element model compared to the model for the applied mass. The comparisons of the reference solution and the prediction according to the energy approach for the first four mode shapes are shown in Figures 5.4, 5.5, 5.6 and 5.7 .

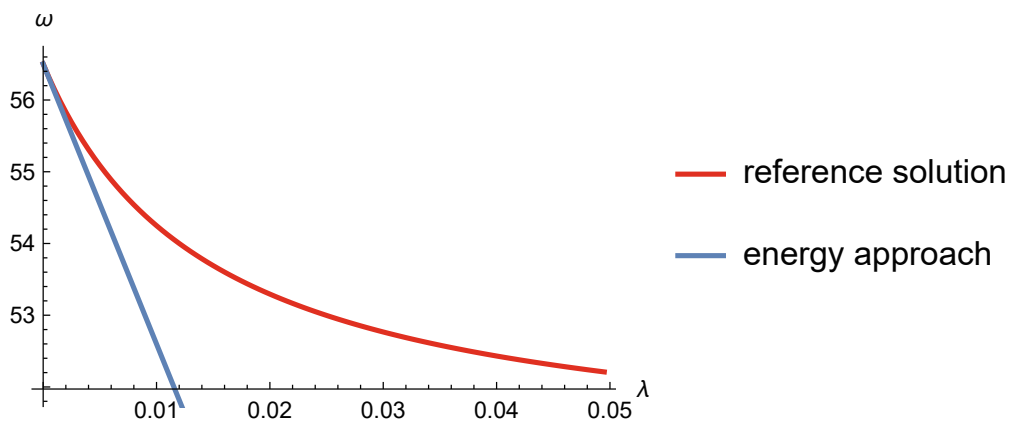


Figure 5.4: Centric crack: reference solution vs. energy approach, mode shape 1

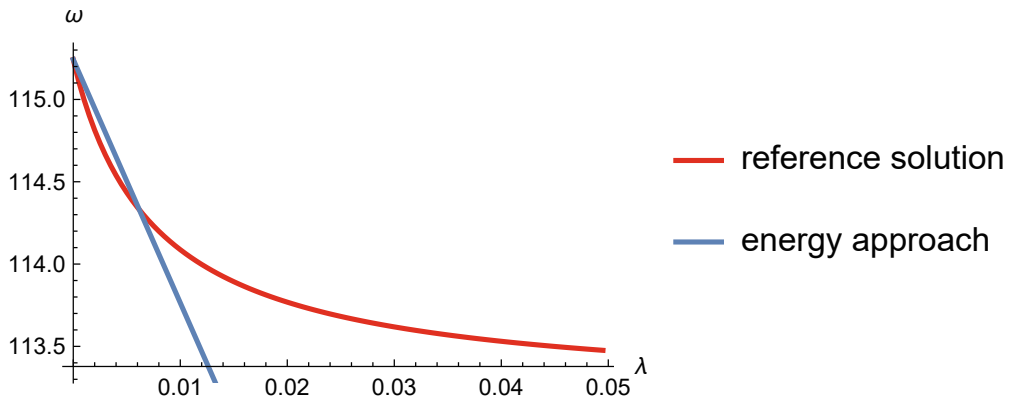


Figure 5.5: Centric crack: reference solution vs. energy approach, mode shape 2

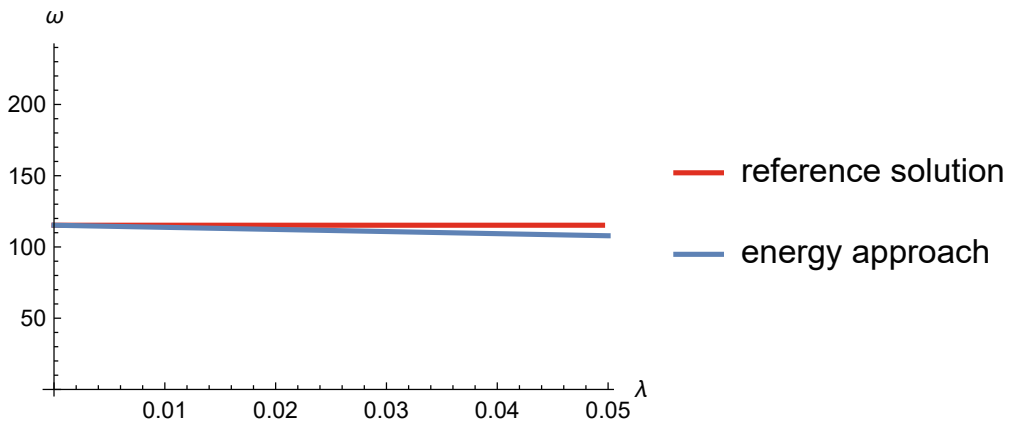


Figure 5.6: Centric crack: reference solution vs. energy approach, mode shape 3

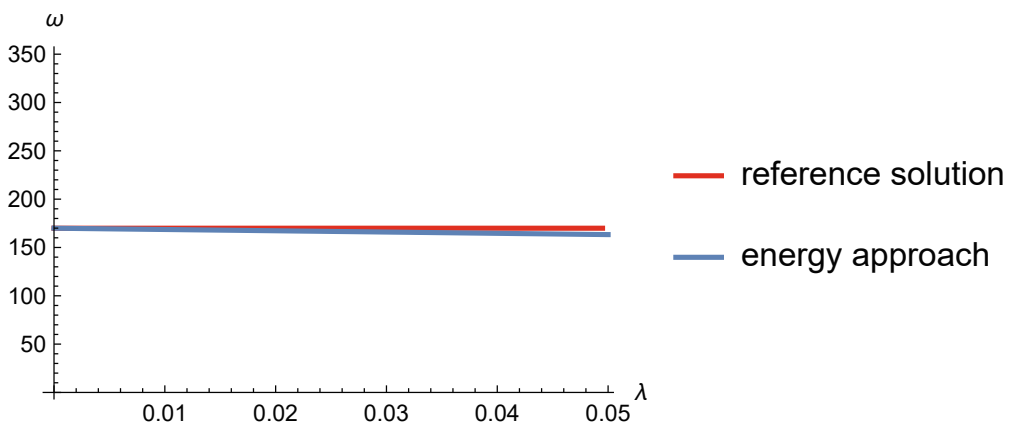


Figure 5.7: Centric crack: reference solution vs. energy approach, mode shape 4

Table 5.2: Convergence study: initial slope - centric crack, mode shape 1

	Number of elements and solution method			
	16 × 16		32 × 32	
	reference	energy approach	reference	energy approach
<b>Initial slope</b>	-384.267	-394.247	-390.327	-390.470

Obviously the first mode shape is repeatedly approximated very good. By the examination of the initial slopes of both solutions in mode shape one, the good correspondence is also seen numerically, see Table 5.2. As initial slopes the first derivatives of the frequency with respect to the compliance value  $\lambda$  for  $\lambda = 0$  are meant. Compared to the plate with added line mass the numerical correspondence between reference solution and energy approach for a small amount of elements was a bit worse. Thus, it was mentioned above that the convergence is a bit slower compared to the model for the line mass. Anyway, with  $32 \times 32$  elements the correspondence is quite good. Furthermore, one clearly sees that the energy approach fails again at the repeated natural frequency two. Surprisingly the third eigenvalue is approximated very good. As expected the fourth eigenvalue is also predicted very good by the energy approach.

An interesting fact is that the natural frequency in the reference solution of mode shape three and four is not influenced by the crack. Hence these reference solutions are displayed by a horizontal line. The question arises, why the fourth eigenvalue is not influenced by the crack. To get to the bottom of this, we examine the bending moment  $M_{yy} = M_{22}$  of the unperturbed plate (used in the complementary energy  $U^*$  in the energy approach) in more detail. To do this, we evaluate the bending moment  $M_{yy}$  all over the plate and plot it three-dimensional, see Figure 5.8. Here additionally a zero-plane ( $z = 0$ ) is displayed in light blue and the crack position is visualized with a red line. According to this figure, the answer to this interesting behaviour of eigenmode four is found. Along the crack length the bending moment is nearly equal to zero, which results further in almost zero complementary energy  $U^*$ .

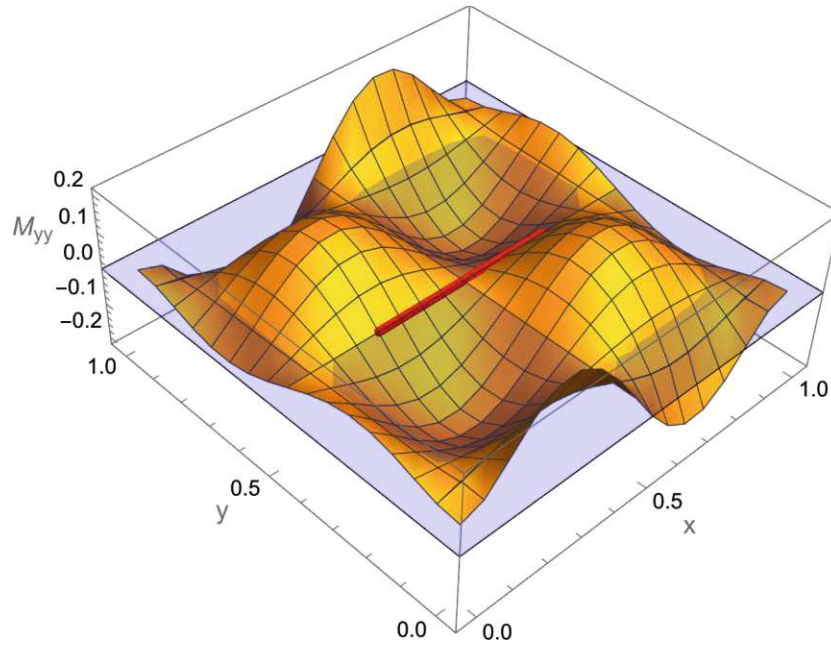


Figure 5.8: Unperturbed plate: bending moment  $M_{yy}(x, y)$ , mode shape 4

### 5.3 Skewed crack

The last simulation of this thesis is the clamped square plate under the influence of a skewed crack ( $\alpha = \pi/6$  to the center), sketched in Figure 5.9. For the reference solution we have to use the skewed mesh again, where the crack is aligned with the element edges.

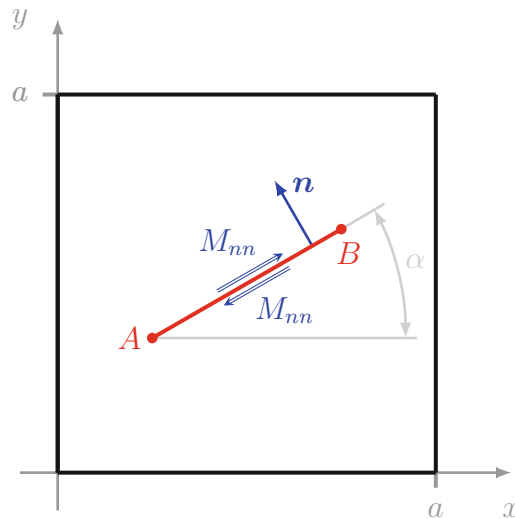


Figure 5.9: Sketch of the skewed crack with normal vector  $\mathbf{n}$  and bending moment  $M_{nn}$

The prediction according to the energy approach (5.1) is evaluated with the rectangular mesh as usual. As with the centric crack, only a higher amount of finite elements yield good correspondence of both solutions. Therefore, we chose for both solution methods a fine mesh with  $24 \times 24$  elements. With this amount of elements the simulation succeeds within a reasonable amount of time. In addition, first troubles with a standard computer occurred with  $32 \times 32$  elements, as in the centric case.

### 5.3.1 Potential of the spring and complementary energy

For the reference solution and energy approach of the skewed crack, we need to determine the elastic energy  $U_s$  as well as the complementary energy  $U^*$  of the rotational spring. We start with  $U_s$  which reads with the normal vector  $\mathbf{n} = -\sin(\alpha)\mathbf{i} + \cos(\alpha)\mathbf{j}$  as

$$U_s = \frac{1}{2}c_T \int_L \left[ \underbrace{\left( \frac{2}{h} \mathbf{J}^{-T} \nabla_{\xi_1 \eta_1} w(\xi_1, \eta_1) \cdot \mathbf{n} \right)}_{\nabla_{xy} w(\xi_1, \eta_1)} \right]_1 - \left( \frac{2}{h} \mathbf{J}^{-T} \nabla_{\xi_1 \eta_1} w(\xi_1, \eta_1) \cdot \mathbf{n} \right)_2 \right]^2 ds. \quad (5.5)$$

Here the directional derivatives  $\nabla_{xy} w(\xi_1, \eta_1) \cdot \mathbf{n}$  are calculated at the shores of the crack and again distinguished with indices one and two. The crack length  $L = \overline{AB}$  (see Figure 5.9) was chosen such that  $L \cos(\alpha) = 0.5a$ . With determined  $U_s$  we are able to calculate the global mass and stiffness matrix and further the eigenvalue problem (reference solution) of the cracked plate. The first four mode shapes of the plate with a skewed crack are depicted in Figure 5.10.

In the next step the complementary energy of the spring  $U^*$  for the skewed crack, which is used in the energy approach, is determined. As in the centric case, the tensor of moments  $\mathbf{m}$  of the unperturbed plate (2.21) is needed. The relevant component of  $\mathbf{m}$  for the skewed crack is the transformed bending moment  $M_{22} = M_{nn} = \mathbf{n} \cdot \mathbf{m} \cdot \mathbf{n}$  which is to be determined along the location of the crack (unperturbed finite element model). For simplicity, here no distinction between upper and lower shore at the crack was made, see Figure 5.9. The complementary energy  $U^*$  of the rotational spring is then given by

$$U^* = \frac{1}{2} \int_L (\mathbf{n} \cdot \mathbf{m} \cdot \mathbf{n})^2 \lambda ds, \quad (5.6)$$

where  $\lambda = 1/c_T$  is the small compliance due to the rotational spring. This integral was evaluated using the trapezoidal rule. Kinetic energy  $T$  and bending strain energy  $U_b$  are calculated according to Equation (3.18). Now all quantities are known and the reference solution as well as the energy approach for the skewed crack are evaluated.

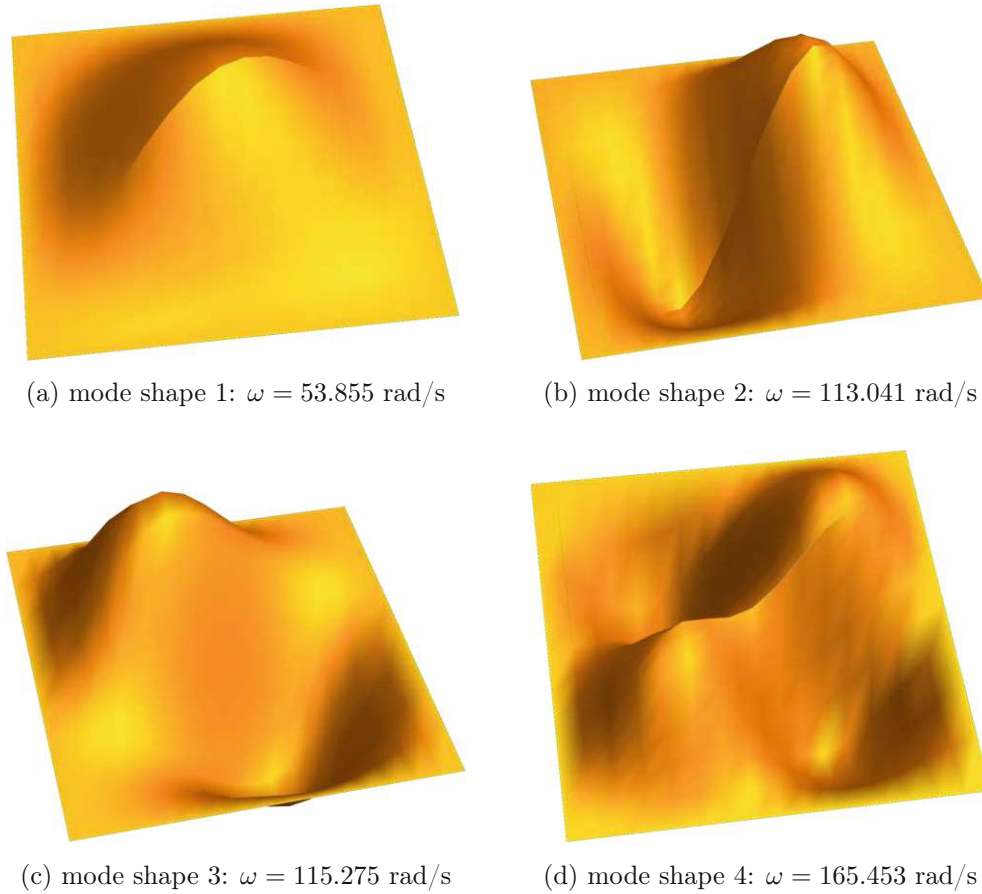


Figure 5.10: Skewed crack: first four mode shapes, skewed mesh  $16 \times 16$  hidden,  $c_T = 10^2$

### 5.3.2 Comparison of reference solution and energy approach

In this section the comparisons of the obtained reference solution and energy approach are presented for the first four mode shapes, see Figures 5.11, 5.12, 5.13 and 5.14. The reference solution is again approximated very well in the first mode shape. As with the centric crack, the numerical correspondence of the initial slopes for the first eigenmode is quite good, see Table 5.3. The skewed crack also clearly shows the failure of the energy approach at the repeated natural frequency two and three. In these mode shapes, the predictions of the energy approach are totally wrong. It seems even that the solution of the energy approach from mode shape three would better fit to reference solution of eigenmode two and vice versa. Another interesting point is that the natural frequency in eigenmode three is not influenced by the crack. In mode shape four the correspondence between both solutions is again quite good.

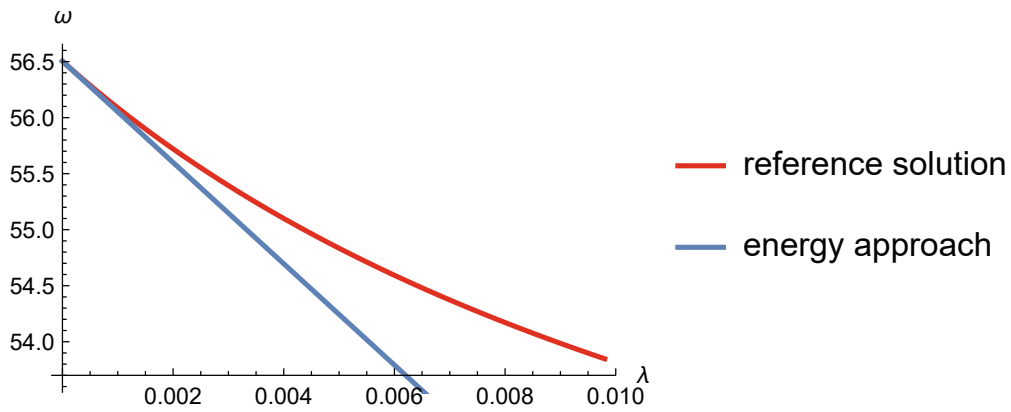


Figure 5.11: Skewed crack: reference solution vs. energy approach, mode shape 1

Table 5.3: Convergence study: initial slope - skewed crack, mode shape 1

	Number of elements and solution method			
	16 × 16		24 × 24	
	reference	energy approach	reference	energy approach
<b>Initial slope</b>	-448.551	-451.984	-452.177	-451.917

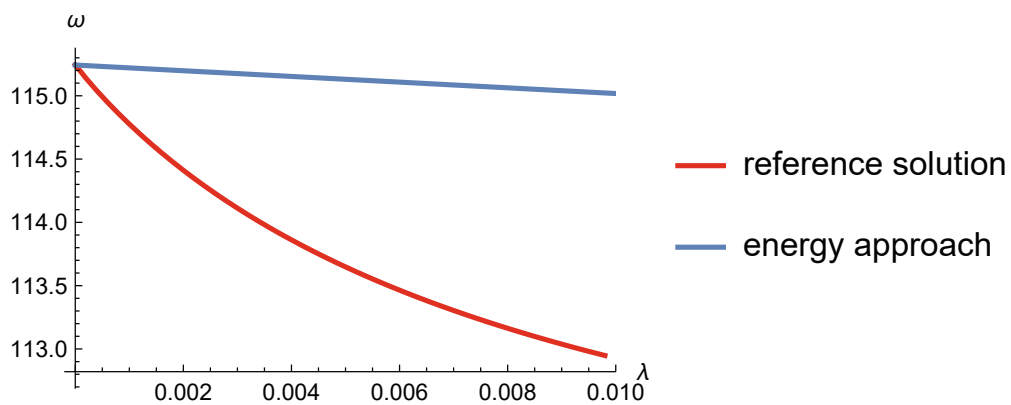


Figure 5.12: Skewed crack: reference solution vs. energy approach, mode shape 2

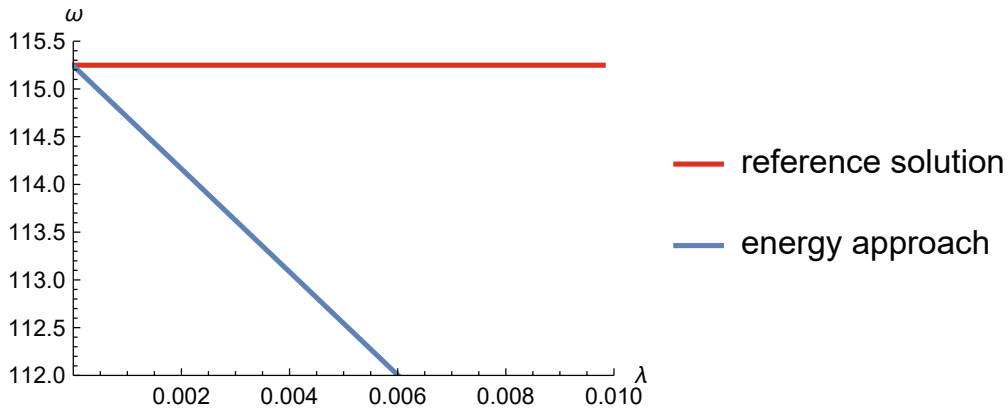


Figure 5.13: Skewed crack: reference solution vs. energy approach, mode shape 3

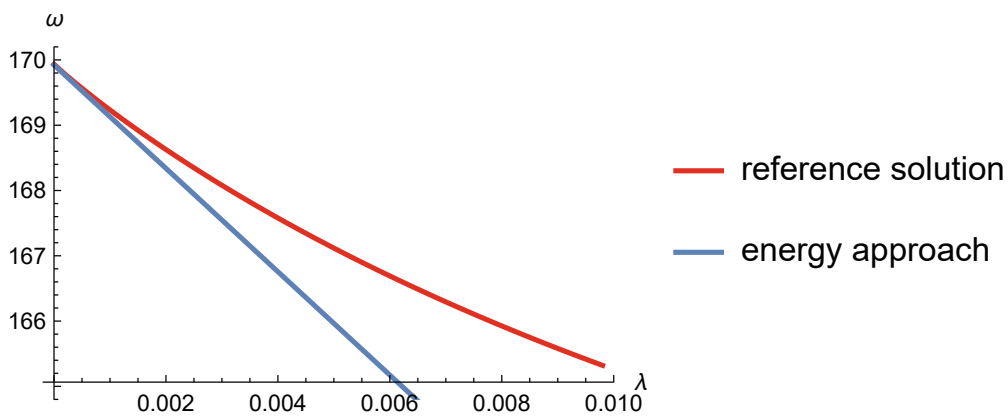


Figure 5.14: Skewed crack: reference solution vs. energy approach, mode shape 4

To sum up, natural frequencies of a cracked plate can only be approximated by the energy approach for unique eigenvalues. At repeated eigenvalues the energy approach in its simple fails. The same behaviour was noticed at the plate with added line mass. Due to this failure of the energy approach in two different plate problems it seems that this previously known formula loses its validity at repeated natural frequencies and requires further extension.

## 6 Conclusion and Outlook

This master thesis deals with natural frequencies of a square plate clamped at all four edges under the influence of a non-through-thickness crack and an applied line mass. The crack and the applied mass result in a variation of stiffness and inertial properties of the plate, which yields a shift in natural frequencies. Using energetic considerations, a general linear approximation can be found to predict such frequency shifts between an origin and perturbed elastic structure, which constitutes the so-called energy approach. Such prediction methods have also a practical significance for the non-destructive inspection of elastic systems (e.g. plate-like structures in machine coverings/casings) using frequency measurement [11]. Changes in natural frequencies are highly dependent on the location and severity of the damage and therefore used to detect and characterise it [11].

During the 13<sup>th</sup> International Symposium on Vibrations of Continuous Systems, which took place in Canada in 2023 [15], the energy approach was treated analytically for simply supported rectangular plates with cracks as well. This awakened motivation to examine the energy approach further for plates with more complex boundary conditions, where the natural vibrations cannot be described by simple analytical expressions. As a result, the prediction according to the energy approach has to be obtained by a chosen numerical method, the finite element method. The advantage of the numerical approach is that for a given set of mode shapes, obtained using a simple regular mesh, one computes changes in the eigenfrequencies for different distribution of additional mass or damage by simple post-processing. The goal of this thesis was to check the energy approach in different mode shapes for a clamped square plate with a crack or added line mass by using the finite element method. In particular, the behaviour of the frequency shift in dependence on the measure of the structural change was determined by means of a traditional analysis using conforming finite element discretization and compared against the predictions obtained by the energy approach.

Wolfram Mathematica was chosen as the simulation environment, where a finite element model was implemented using Bogner-Fox-Schmit approximation. At first, a line mass

along the element edges was applied and tested. Therefore, two meshes, a rectangular and a skewed one, were needed to apply the mass at an arbitrary angle  $\alpha$  and obtain the reference solution. Moreover, a convergence study of these two meshes was also conducted. Afterwards, the square plate was simulated with a crack (centric and skewed) along element edges. The crack was modelled by creating new degrees of freedom and adding a rotational spring along its length. For each case, applied mass or crack, the reference solution for the frequency shift was determined and presented together with the solution obtained by the energy approach (first four mode shapes).

The main outcome of this thesis is that the previously known formula for the energy approach fails at repeated natural frequencies, as they occur with square and clamped plates. It is obvious that in mode shape two and three (repeated eigenvalue) the solution of the energy approach does not approximate the reference solution. The initial slopes of both dependencies of the eigenfrequency on the imperfection parameter are different. For unique natural frequencies the reference solution can be predicted very well by the energy approach. Additionally, convergence is shown numerically for the first eigenmode. As a result, the following question occurs: Does the possibility exist to modify the previously known formula for the energy approach to cover repeated natural frequencies as well? The answer to this question could be the subject of future mechanical endeavors.

# List of Figures

2.1	Sketch of a plate problem . . . . .	3
2.2	Kinematic assumptions for the plate problem . . . . .	6
2.3	The system is discretized using finite elements . . . . .	13
2.4	Mapping from local to global coordinates (plate problem) . . . . .	18
2.5	Beam with added mass: exact solution vs. energy approach, mode shape 1	22
3.1	Square BFS-element with nodal DOFs and local coordinate system $\xi - \eta$	23
3.2	One-dimensional cubic Hermitian polynomials for shear rigid beam elements . . . . .	24
3.3	Bi-cubic shape functions of node 1 of a Bogner-Fox-Schmit element . . . . .	25
3.4	Rectangular mesh and mapping . . . . .	26
3.5	First four mode shapes with rectangular $4 \times 4$ mesh . . . . .	27
3.6	Mapping from local to global coordinates (skewed element) . . . . .	28
3.7	Sketch to point out the problem with the $\mathcal{C}^1$ -continuity . . . . .	29
3.8	Sketch for the $\mathcal{C}^1$ -continuous mapping $(\xi, \eta) \rightarrow (x, y)$ . . . . .	30
3.9	$\mathcal{C}^1$ -continuous mapping $\eta \rightarrow y$ . . . . .	31
3.10	$\mathcal{C}^1$ -continuous mapping from the FE mesh into the physical domain . . . . .	31
3.11	Convergence study . . . . .	33
3.12	Convergence study, enlarged . . . . .	33
4.1	Centric line mass - plot on the first two eigenmodes . . . . .	35
4.2	Centric line mass: reference solution vs. energy approach, mode shape 1	36
4.3	Relative error: centric line mass, mode shape 1 . . . . .	36
4.4	Centric line mass: reference solution vs. energy approach, mode shape 2	37
4.5	Centric line mass: reference solution vs. energy approach, mode shape 3	37
4.6	Centric line mass: reference solution vs. energy approach, mode shape 4	37
4.7	Skewed line mass - plot on the first two eigenmodes . . . . .	39
4.8	Skewed line mass: reference solution vs. energy approach, mode shape 1	39
4.9	Skewed line mass: reference solution vs. energy approach, mode shape 2	40

4.10 Skewed line mass: reference solution vs. energy approach, mode shape 3	40
4.11 Skewed line mass: reference solution vs. energy approach, mode shape 4	40
5.1 Mechanical modelling: non-through-thickness crack . . . . .	42
5.2 Crack implementation in the FE-model - split up degrees of freedom . .	43
5.3 Centric crack - comparison of static deflection, hidden rectangular mesh .	45
5.4 Centric crack: reference solution vs. energy approach, mode shape 1 . .	46
5.5 Centric crack: reference solution vs. energy approach, mode shape 2 . .	47
5.6 Centric crack: reference solution vs. energy approach, mode shape 3 . .	47
5.7 Centric crack: reference solution vs. energy approach, mode shape 4 . .	47
5.8 Unperturbed plate: bending moment $M_{yy}(x, y)$ , mode shape 4 . . . . .	49
5.9 Sketch of the skewed crack with normal vector $\mathbf{n}$ and bending moment $M_{nn}$ . . . . .	49
5.10 Skewed crack: first four mode shapes, skewed mesh $16 \times 16$ hidden, $c_T =$ $10^2$ . . . . .	51
5.11 Skewed crack: reference solution vs. energy approach, mode shape 1 . .	52
5.12 Skewed crack: reference solution vs. energy approach, mode shape 2 . .	52
5.13 Skewed crack: reference solution vs. energy approach, mode shape 3 . .	53
5.14 Skewed crack: reference solution vs. energy approach, mode shape 4 . .	53

# List of Tables

2.1	Gauss-Legendre parameters [10] . . . . .	19
3.1	Convergence study: skewed - rectangular mesh . . . . .	34
4.1	Convergence study: initial slope - centric line mass, mode shape 1 . . . . .	38
4.2	Convergence study: initial slope - skewed line mass, mode shape 1 . . . . .	41
5.1	Convergence study: max. static deflection, $32 \times 32$ elements . . . . .	46
5.2	Convergence study: initial slope - centric crack, mode shape 1 . . . . .	48
5.3	Convergence study: initial slope - skewed crack, mode shape 1 . . . . .	52

# Bibliography

- [1] Steindl Alois, Buchta Roman, Ruttmann Michael, and Vetyukov Yury. “Numerical Investigations of Large Amplitude Oscillations of Planar Parametrically Excited Beams”. In: *Progress in Continuum Mechanics*. Ed. by Altenbach Holm, Irschik Hans, and Porubov Alexey V. Springer Nature Switzerland, 2023, pp. 411–428. ISBN: 978-3-031-43736-6. URL: [https://doi.org/10.1007/978-3-031-43736-6\\_24](https://doi.org/10.1007/978-3-031-43736-6_24).
- [2] Holm Altenbach. *Kontinuumsmechanik : Einführung in die materialunabhängigen und materialabhängigen Gleichungen*. ger. 4., korrigierte und überarbeitete Auflage. Berlin: Springer Vieweg, 2018. ISBN: 3662575043.
- [3] Holm Altenbach, Johannes Altenbach, and Konstantin Naumenko. *Ebene Flächen-tragwerke: Grundlagen der Modellierung und Berechnung von Scheiben und Platten*. Berlin Heidelberg: Springer Berlin Heidelberg: Springer Vieweg, 2023. ISBN: 3662683911.
- [4] K Bhaskar and T. K Varadan. *Plates : Theories and Applications*. eng. 1st ed. 2021. Cham: Springer International Publishing Imprint: Springer, 2021. ISBN: 3030694240.
- [5] Clarence W De Silva. *Vibration : fundamentals and practice*. eng. Boca Raton, Fla. [u.a.]: CRC Press, 2000. ISBN: 0849318084.
- [6] S. Eisenträger, J. Kiendl, G. Michaloudis, R. Duy, and Y. Vetyukov. “Stability analysis of plates using cut Bogner-Fox-Schmit elements”. eng. In: *Computers & structures* 270 (2022), p. 106854. ISSN: 0045-7949.
- [7] Bogner F.K., Fox R.L., and Jr. Schmit L.A. “The generation of interelement compatible stiffness and mass matrices by the use of interpolation formulae”. In: *Proceedings of the 1st conference on matrix methods in structural mechanics* (1965), pp. 397–444.

- [8] Robert Gasch, Klaus Knothe, and Robert Liebich. *Strukturodynamik : Diskrete Systeme und Kontinua*. ger. 2. Aufl. 2012. Berlin, Heidelberg: Springer Berlin Heidelberg, 2012. ISBN: 3540889779.
- [9] P. Gudmundson. “Eigenfrequency changes of structures due to cracks, notches or other geometrical changes”. eng. In: *Journal of the mechanics and physics of solids* 30.5 (1982), pp. 339–353. ISSN: 0022-5096.
- [10] Manfred Hahn and Michael Reck. *Kompaktkurs Finite Elemente für Einsteiger: Theorie und Beispiele zur Approximation linearer Feldprobleme*. ger. Wiesbaden: Springer Fachmedien Wiesbaden: Springer Vieweg, 2018. ISBN: 3658227753.
- [11] Logesh Kannappan and Krishna Shankar. “Non destructive inspection of plates using frequency measurements”. In: (Jan. 2007). URL: [https://www.researchgate.net/publication/43476755\\_Non\\_destructive\\_inspection\\_of\\_plates\\_using\\_frequency\\_measurements](https://www.researchgate.net/publication/43476755_Non_destructive_inspection_of_plates_using_frequency_measurements).
- [12] Klaus Knothe and Heribert Wessels. *Finite Elemente : Eine Einführung für Ingenieure*. ger. 5. Aufl. 2017. Berlin, Heidelberg: Springer Berlin Heidelberg Imprint: Springer Vieweg, 2017. ISBN: 3662493527.
- [13] Michael Krommer. *Mechanik 3*. Lecture notes TU Wien, LVA Nr. 301.036, Sommersemester 2019.
- [14] A.W. Leissa. “The free vibration of rectangular plates”. In: *Journal of sound and vibration* 31.3 (1973), pp. 257–293. ISSN: 0022-460X.
- [15] F. Masoudian, A. A. Satpute, D. Kennedy, C. A. Featherston, and S. Ilanko. “Natural Frequencies of Cracked Rectangular Plates: An Energy Approach”. In: *ISVCS 2023 – Proceedings of 13th International Symposium on Vibrations of Continuous Systems*. 2023, pp. 33–35. URL: [http://www.isvcs.org/ISVCS13\\_Alberta\\_Canada\\_2023.pdf](http://www.isvcs.org/ISVCS13_Alberta_Canada_2023.pdf).
- [16] Christian Mittelstedt. *Theory of Plates and Shells*. eng. 1st ed. 2023. Berlin Heidelberg: Springer Berlin Heidelberg: Springer Vieweg, 2023. ISBN: 366266805X.
- [17] Heinz Pettermann and Jan Kaul. *Einführung in die Finite Elemente Methoden*. Lecture notes TU Wien, LVA Nr. 317.016, Wintersemester 2019.
- [18] Melanie Todt and Pavan Kumar Asur Vijaya Kumar. *Nonlinear Finite Element Method*. Lecture notes TU Wien, LVA Nr. 317.535, Wintersemester 2023.

- [19] Y. Vetyukov. “Finite element modeling of Kirchhoff-Love shells as smooth material surfaces”. In: *Zeitschrift für angewandte Mathematik und Mechanik* 94.1-2 (2014), pp. 150–163. ISSN: 0044-2267.
- [20] Yury Vetyukov. *Mechanik 3*. Lecture notes TU Wien, LVA Nr. 301.036, Sommersemester 2020.
- [21] Yury Vetyukov and Michael Krommer. *Höhere Festigkeitslehre*. Lecture notes TU Wien, LVA Nr. 325.064, Wintersemester 2021.
- [22] Inc. Wolfram Research. *Mathematica, Version 13.3.1*. Champaign, IL, 2023. URL: <https://www.wolfram.com/mathematica>.
- [23] O. C. Zienkiewicz and Robert L. Taylor. *The Finite Element Method Set*. eng. 6th ed. Burlington: Elsevier Science, 2013. ISBN: 1282381342.